RSC Advances

PAPER

View Article Online
View Journal | View Issue

Cite this: *RSC Adv.*, 2026, **16**, 3662

Enhanced sensing characteristics of N doped and (N, O) co-doped molybdenum disulfide to detect toxic gases: a comprehensive first-principles study

Khiet An Vuong,[a] Nguyen Hai Dang,[b] Le Phuong Truong,[c] Minh-Thuan Pham,[d] D. M. Hoat,[ef] Minh Triet Dang,[g] Guo-Ping Chang-Chien[d] and Duy Khanh Nguyen *[hi]

First-principles calculations based on density functional theory were conducted to investigate the adsorption of CO, CO_2, and NH_3 molecules on pristine, N doped, and (N, O) co-doped MoS_2 surfaces. Pristine MoS_2 systems exhibit weak physisorption with long adsorption distances, insignificant adsorption energies, and negligible charge transfer, resulting in poor gas selectivity and low electronic sensitivity toward all gases. N doping slightly enhances adsorption strength and charge exchange through defect-induced electronic modulation, improving the interaction with NH_3 but showing limited response to CO and CO_2. In contrast, (N, O) co-doping substantially reinforces molecule–substrate interactions by reducing adsorption distances and increasing charge redistribution across the surface. The (N, O) co-doped MoS_2 system exhibits pronounced work-function shifts of −1.07, −0.99, and −0.54 eV for CO, CO_2, and NH_3, respectively, together with strong energy-resolved conductivity variations, with average conductivity changes of about 30–40% for CO, 35–50% (peaks ≈70%) for CO_2, and 45–60% with maximum peaks exceeding 120% for NH_3. Compared with previous studies focusing on either N- or O-doped MoS_2, our work provides a systematic, side-by-side comparison of pristine, N-doped, and (N, O) co-doped systems and identifies (N, O) co-doping as a more effective route to simultaneously enhance sensitivity and selectivity toward CO and CO_2.

Received 20th November 2025
Accepted 22nd December 2025

DOI: 10.1039/d5ra08975a

rsc.li/rsc-advances

1. Introduction

With the immense advances of our society, air pollution caused by hazardous gases such as carbon monoxide (CO), carbon dioxide (CO_2), and ammonia (NH_3) has become a critical global issue, threatening both environmental security and human health.[1–3] Long-term exposure to these molecules can trigger severe respiratory problems and ecological imbalance, while accidental leakage in industrial facilities poses additional safety risks. This highlights the urgent demand for advanced sensing platforms capable of detecting these gases with high precision, fast response, and strong selectivity. The integration of gas sensors with the "Internet of Things" has opened new opportunities for real-time monitoring and smart environmental management, yet the performance of conventional materials remains constrained by limited sensitivity, selectivity, and stability.[4] Among the materials suitable for toxic gas sensors, two-dimensional (2D) materials have attracted considerable attention in recent years due to their unique physical and chemical properties, such as high surface area, tunable band gap, and diverse electronic structures.[5–26] Their ultrathin geometry maximizes the fraction of exposed atoms, providing abundant active sites for adsorption.[27] Moreover, the flexibility in their electronic states enables pronounced modulation of conductivity and band structure upon interaction with gas molecules, making them excellent candidates for sensitive and selective gas sensing.[28] Graphene, a 2D allotrope of carbon atoms discovered by Geim *et al.* Graphene is well known for its exceptional mechanical strength, high electrical conductivity, excellent thermal conductivity, and unique Dirac cone-shaped electronic band structure, which causes electrons (e^-) in graphene to behave like massless particles.[29] This achievement not only opened wide prospects for applications in electronics, sensing, and energy storage, but also laid the foundation for the rapid development of

[a]*School of Natural Sciences, Can Tho University, Can Tho City, Vietnam*
[b]*Faculty of Basic Sciences, Nam Can Tho University, Can Tho City, Vietnam*
[c]*Faculty of Mechatronics and Electronics, Lac Hong University, Dong Nai Province, Vietnam*
[d]*Center for Environmental Toxin and Emerging-Contaminant Research, Cheng Shiu University, Kaohsiung City, Taiwan*
[e]*Institute of Theoretical and Applied Research, Duy Tan University, Ha Noi 100000, Vietnam*
[f]*School of Engineering and Technology, Duy Tan University, Da Nang 550000, Vietnam*
[g]*School of Education, Can Tho University, Can Tho City, Vietnam*
[h]*Laboratory for Computational Physics, Institute for Computational Science and Artificial Intelligence, Van Lang University, Ho Chi Minh City, Vietnam. E-mail: khanh.nguyenduy@vlu.edu.vn*
[i]*Faculty of Mechanical, Electrical, and Computer Engineering, Van Lang School of Technology, Van Lang University, Ho Chi Minh City, Vietnam*

other 2D materials such as silicene and transition metal dichalcogenides (TMDs).[30] Beyond transition-metal dichalcogenides, recent DFT studies have demonstrated that porous and low-dimensional frameworks such as 3D boron–phosphorus–carbon, triphenylene-graphdiyne analogs, and porous borocarbonitrides exhibit highly tunable electronic structures and adsorption properties suitable for gas and ion storage.[31–35] These works highlight the importance of rationally engineering low-dimensional frameworks to control charge transfer and adsorption strength, which motivates the present design of N- and (N, O) doped MoS_2 gas-sensing platforms.

Regarding gases adsorbed 2D systems, our previous report has employed first-principles density functional theory (DFT) calculations to investigate the adsorption of NO and CO molecules on silicene monolayer.[21] They have reported that up to four NO molecules can be chemically adsorbed onto pristine silicene with adsorption energies ranging from −0.32 to −1.22 eV, leading to rich electronic behaviors such as magnetic semiconducting and half-metallicity. In contrast, CO shows only weak physisorption on pristine silicene, with adsorption energies around −0.26 eV, indicating poor sensitivity. However, aluminum (Al) doping significantly enhances CO adsorption, lowering the adsorption energy to between −0.19 and −0.71 eV per molecule, while also inducing either bandgap opening or metallization depending on the adsorption configuration. These findings highlight pristine and Al-doped silicene monolayers as promising candidates for nitric oxide (NO) and CO gas sensing applications. In addition, the study further emphasizes the crucial role of foreign atom doping in tuning the electronic properties and structural characteristics of 2D materials, as well as modulating the gas adsorption process itself by altering charge transfer, adsorption configurations, and binding strengths. Among the broad family of 2D systems, TMDs have drawn particular interest since they exhibit a wide range of electronic behaviors, from metallic to semiconducting, depending on their composition and structural configuration. In 2023, Maciej J. Szary *et al.* employed first-principles DFT calculations based on the Perdew–Burke–Ernzerhof (PBE) exchange-correlation functional with Grimme's D3 dispersion correction to investigate the adsorption behavior of nitrogen dioxide (NO_2) on molybdenum disulfide (MoS_2), molybdenum diselenide ($MoSe_2$), and molybdenum ditelluride ($MoTe_2$) monolayers.[36] The work revealed that NO_2 interacts most strongly with $MoTe_2$, exhibiting the highest charge transfer, whereas $MoSe_2$ shows intermediate adsorption strength and MoS_2 displays the weakest interaction. Despite sharing similar orbital characteristics and outward charge projections, the three materials display distinct adsorption energies and charge transfer values, which are linked to differences in charge accumulation and bonding within the sheets. On average, NO_2 adsorption energy on $MoTe_2$ exceeds that of MoS_2 by more than 160%, and the charge transfer is over six times higher, indicating superior sensing potential for $MoTe_2$ at the expense of slower recovery. In contrast, $MoSe_2$ offers a balanced performance between sensitivity and recovery. These results highlight that the availability of charge on the TMDs surfaces governs adsorption strength, and the findings provide chemical insight into the enhanced interaction of NO_2 with Mo-bearing dichalcogenides.

In particular, MoS_2, one of the most representative TMDs, has attracted considerable attention owing to its remarkable physicochemical properties and broad potential in optoelectronic, catalytic, and gas-sensing applications.[37–40] Unlike graphene, which lacks an intrinsic bandgap, MoS_2 is a semiconductor with an indirect band gap of about 1.2 eV in the bulk and a direct band gap of nearly 1.8 eV in the monolayer.[38] This transition in bandgap, combine with its robust stability and distinctive features such as high surface area, tunable band gap, and diverse electronic structures, makes MoS_2 a highly promising material for high-performance gas sensing devices.[36,39–46] Overall, the pristine MoS_2 generally shows weak adsorption toward nonpolar molecules such as CO and CO_2, which restricts its sensing efficiency.[42] In contrast, NH_3 is a highly polar molecule with a lone electron pair on the nitrogen atom (N), allowing stronger interaction with the MoS_2 surface through charge donation and acceptance.[44] Even so, the adsorption strength remains insufficiently stable and lacks selectivity, which makes reliable NH_3 detection with pristine MoS_2 still challenging. Previous DFT studies have revealed that MoS_2 interacts with various gas molecules through charge-transfer processes,[47–50] thereby modifying its electronic and transport properties. In 2021, Francis M. Enujekwu *et al.*[44], conducted a DFT investigation on CO_2 adsorption over defective and N-doped MoS_2. Their results indicated that a single sulfur (S) vacancy facilitates the dissociative adsorption of CO_2 with high selectivity over N_2 and water (H_2O) molecules, whereas a molybdenum vacancy substituted by three N atoms markedly enhances physisorption, yielding an adsorption energy of −1.818 eV compared with −0.139 eV for pristine MoS_2. Furthermore, vibrational frequency calculations corroborated these findings, confirming that N doping combined with defect engineering is an effective approach to improve both the adsorption capacity and selectivity of MoS_2 toward CO_2.

Although numerous studies in recent years have explored both pristine and heteroatom–doped MoS_2, particularly N and oxygen (O) doping, a truly comprehensive and systematic investigation remains lacking.[44,51] Most existing works have examined the individual influence of N or O incorporation on the electronic, optical, and gas adsorption properties of MoS_2, yet few have provided a consistent comparative analysis elucidating the distinct mechanisms and potential synergy between these dopants. Consequently, a critical knowledge gap persists in understanding how N and O differ in modulating charge transfer, adsorption strength, and selectivity, as well as how their simultaneous incorporation may produce cooperative effects. In this study, (N, O) co-doping emerges as a highly promising strategy, as the coexistence of N and O atoms is expected to generate a synergistic interaction in which N introduces additional active sites and facilitates charge transfer, while O, owing to its higher electronegativity, modifies the local lattice environment and reinforces Mo–O bonding. Such a cooperative effect can effectively optimize sensitivity, selectivity, and stability during gas adsorption, enabling (N, O) co-doped MoS_2 to overcome the inherent limitations of pristine and singly doped systems and offering new opportunities for developing high-performance gas sensors.

2. Computational methods

To investigate the structural, electronic, sensing properties of gas adsorption (CO, CO_2, NH_3) on N doped and (N, O) co-doped MoS_2 systems, the spin-polarized density functional theory (SDFT) is performed using the Vienna *Ab initio* Simulation Package (VASP).[52] All calculations were performed for monolayer 2H–MoS_2 in its trigonal-prismatic phase, which is the thermodynamically stable and experimentally most relevant polymorph for gas-sensing applications.[53] The generalized gradient approximation (GGA) with the Perdew–Burke–Ernzerhof (PBE) functional is used to treat the exchange-correlation.[54] Besides, the intrinsic e^-–ion interactions are characterized through the projector-augmented wave (PAW) pseudopotentials.[55] As to the complete set of plane waves, the kinetic energy cutoff is set to be 500 eV, being suitable for evaluating Bloch wave functions and electronic energy spectra. All calculations were carried out within spin-polarized density functional theory. For each target gas (CO, CO_2, and NH_3), the isolated molecule was first optimized in a large cubic box using the same exchange-correlation functional, plane-wave cutoff, and *k*-point sampling as in the adsorption calculations. The adsorption energies were then evaluated from these relaxed gas configurations. Long-range van der Waals (vdW) corrections beyond PBE were not included; this may lead to a systematic underestimation of the absolute adsorption energies, but the relative trends between pristine, N-doped, and (N, O) co-doped MoS_2 are expected to be robust. To achieve the free-standing monolayer, a vacuum space of 10 Å is inserted between each monolayer, which is contained a box height of 20 Å. Then, a $2 \times 2 \times 1$ supercell along *a*, *b*, and *c*-axis directions were built which contained 12 atoms. During the structural optimizations, only the internal atomic coordinates were relaxed, while the lattice vectors, including the vacuum spacing along the *z*-direction, were kept fixed. This supercell size represents a compromise between computational cost and accuracy and is consistent with previous first-principles gas-sensing studies on 2D materials.[56,57] The first Brillouin zone is sampled by $5 \times 5 \times 1$ and $30 \times 30 \times 1$ *k*-point meshes within the *Γ*-centered scheme for geometric optimizations and self-consistent calculations, respectively. The energy convergence is equal to 10^{-5} eV between two consecutive steps, and the maximum Hellmann–Feynman force acting on each atom is less than 0.01 eV $Å^{-1}$ during the ionic relaxations. In addition, it should be noted that how to choose the reasonable *k*-point mesh and ENCUT value is a critical factor to balance between the computational cost and accuracy. To address this issue, we have carefully investigated convergence of various *k*-point meshes ($5 \times 5 \times 1$, $7 \times 7 \times 1$, $9 \times 9 \times 1$, and $11 \times 11 \times 1$) and ENCUT values (500 eV, 550 eV, 600 eV, 650 eV), in which variation of adsorption energy (E_{ads}) and work function (WF) values with the aforementioned *k*-point meshes and ENCUT values has been rigorously evaluated, as provided in Tables S1–S4 in the SI. As a result, the variation of the E_{ads} and WF values with respect to the different *k*-point meshes and ENCUT values is smaller than the reasonable threshold: *e.g.*, 0.001–0.028 eV for WF and 0.000001–0.000002 eV for E_{ads} (Tables S1 and S2), and 0.001–0.028 eV for WF and 0.00003 eV for E_{ads} (Tables S3 and S4). This evidences that the chosen $5 \times 5 \times 1$ *k*-point mesh and ENCUT of 500 eV is a great compromise between computational cost and accuracy.

3. Results and discussion

3.1. Geometric structure

Pristine MoS_2 consists of Mo and S atoms arranged in three distinct atomic planes, forming a sandwich-like S–Mo–S structure, as shown in Fig. 1(a). We construct the geometric structure of the MoS_2 lattice as a $2 \times 2 \times 1$ supercell as the basis for investigating the adsorption behavior of CO, CO_2, and NH_3 molecules. This supercell contains 12 atoms (4 Mo and 8 S). Substituting one S atom by N corresponds to a doping concentration of $1/12 \approx 8.3\%$, whereas replacing two S atoms by N and O yields a (N, O) co-doping level of $2/12 \approx 16.7\%$. In optimal state, the geometric structure of pristine MoS_2 is characterized with a surface corrugation of 1.564 Å, stable Mo–S bond lengths of 2.413 Å, a buckling height is 1.564 Å. In this study, a total of 25 possible configurations were examined for the adsorption of CO, CO_2, and NH_3 on MoS_2 surface at representative adsorption sites. The typical gases adsorption sites include: A (gases on top of an S atom), B (gases on bridge site between Mo and S), C (gases on center of the six-membered ring of MoS_2), and D (gases on top of a Mo atom), observed along the *z*-axis, as illustrated by Fig. 1(a). Specifically, site A_1 is an A-type site where the carbon atom of CO/CO_2 or the N atom of NH_3 points down toward the MoS_2, N doped MoS_2 (N–MoS_2), or (N, O) co-doped MoS_2 (N–O–MoS_2) substrate. Likewise, site A_2 is an A-type site where the O atom of CO/CO_2 or the hydrogen atom of NH_3 points down toward the substrate. In the same manner, the B_1, B_2, C_1, C_2, D_1, and D_2 sites are defined the same manner as illustrated by Fig. S1–S3 in the SI data. In addition, for CO we also examine one more configuration called A_3, which is the A-type site with the CO molecule lying parallel to the *z*-axis (horizontally with respect to *z*).

Since MoS_2 is a 2D material, a vacuum layer of approximately 20 Å was introduced along the *z*-direction to avoid spurious interactions between periodic images. The initial adsorption distance between the gas molecule and the surface was set to 3 Å for all configurations. Specifically, 25 possible adsorption configurations of pristine MoS_2 including 9 for CO, 8 for CO_2, and 8 for NH_3. Under optimal calculations, all the most stable adsorption configurations of the pristine MoS_2, (N) doped MoS_2, and (N, O) co-doped MoS_2 systems are shown in Fig. 1(a–l), respectively.

The structural and electronic characteristics of pristine-MoS_2 system were analyzed through adsorption energy (E_{ads}), adsorption distance (*d*), surface corrugation (*h*), the longest and shortest Mo–S bond lengths (1st Mo–S and 2nd Mo–S), and the electronic bandgap or metallic state (bandgap/metal), and work function. The optimized geometric parameters are displayed in Table 1. Among these, the adsorption energy E_{ads} indicates the binding strength and stability of the system, whereas a more negative value reflects a more stable adsorption. Thus, negative E_{ads} values indicate exothermic and thermodynamically favorable adsorption, whereas positive E_{ads} values correspond to

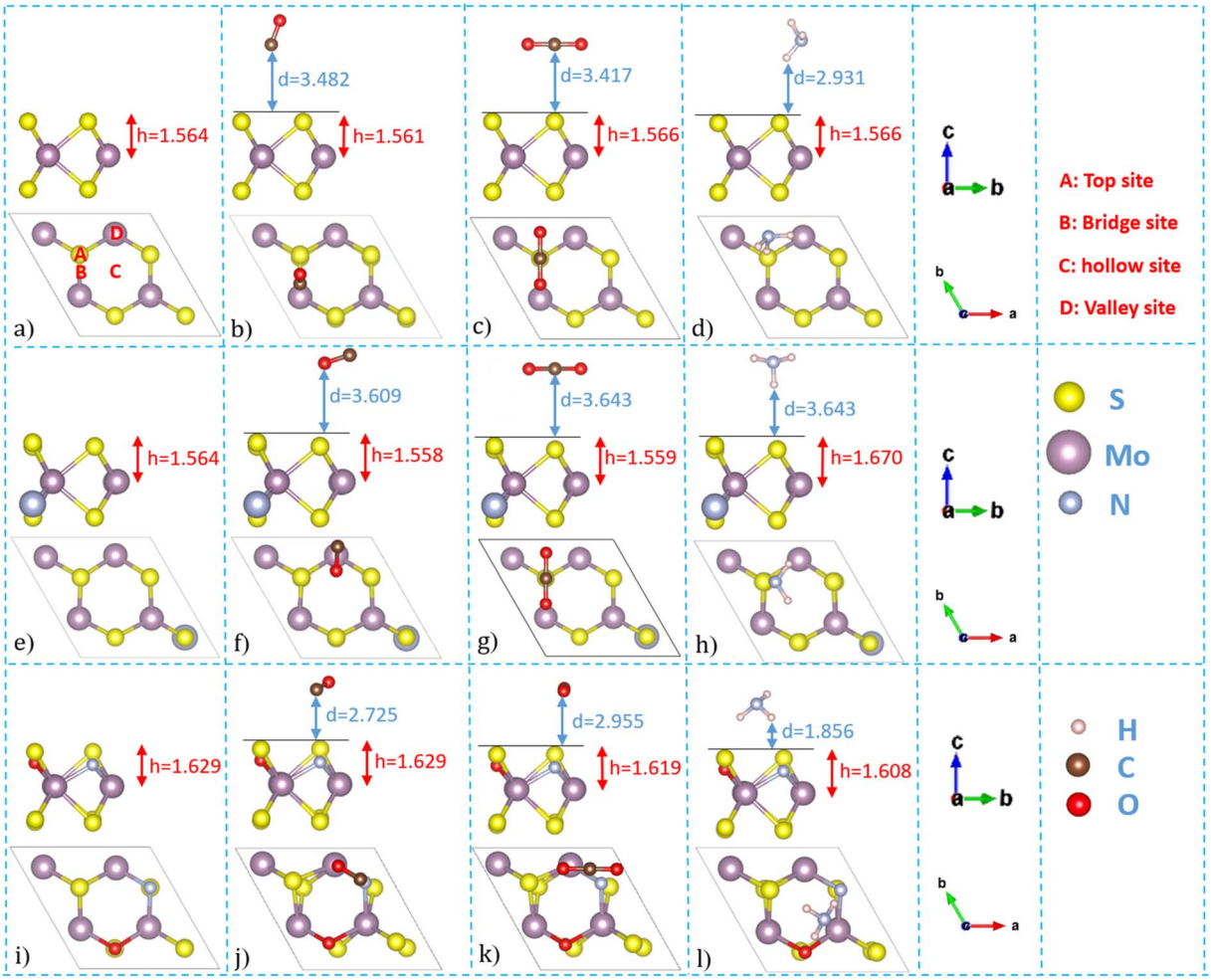

Fig. 1 Optimal structure of (a) pristine-MoS_2, (b) MoS_2–CO–B_1, (c) MoS_2–CO_2–A_1, (d) MoS_2–NH_3–A_1, (e) N–MoS_2, (f) N–MoS_2–CO–D_1, (g) N–MoS_2–CO_2–A_1, (h) N–MoS_2–NH_3–A_1, (i) N–O–MoS_2, (j) N–O–MoS_2–CO–D_1, (k) N–O–MoS_2–CO_2–D_1, (l) N–O–MoS_2–NH_3–D1. The notations A_1, B_1, and D_1 refer to adsorption sites for the target gases (detailed in Fig. S1), whereas the buckling height (h) and distances from gases to substrate (d) are measured by unit in Å.

Table 1 Optimal structural parameters, adsorption energy (E_{ads}), adsorption distance (d), buckling height (h), and Mo–S longest (1st Mo–S) and shortest (2nd Mo–S) bond lengths, bandgap/metal, work function (ϕ), and magnetic moment (μ_B) of the pristine-MoS_2, N–MoS_2 and N–O–MoS_2 before and after CO, CO_2, and NH_3 adsorption, whereas the zero magnetic moment (μ_B) stands for the non-magnetism

Configuration	E_{ads} (eV)	D (Å)	h (Å)	1st Mo–S (Å)	2nd Mo–S (Å)	Bandgap (eV) per metal	ϕ (eV)	Magnetic moment (μ_B)
Pristine-MoS_2	X	X	1.564	2.413	2.412	1.77	5.525	0
MoS_2–CO–B_1	−0.15	3.482	1.561	2.413	2.411	1.69	5.637	0
MoS_2–CO_2–A_1	−0.15	3.417	1.566	2.415	2.412	1.69	6.584	0
MoS_2–NH_3–A_1	−0.18	2.931	1.566	2.413	2.412	1.68	5.701	0
N–MoS_2	X	X	1.595	2.418	2.405	Metal	5.648	0
N–MoS_2–CO–D_1	−0.02	3.609	1.558	2.416	2.416	Metal	5.508	0
N–MoS_2–CO_2–A_1	−0.02	3.643	1.559	2.416	2.414	Metal	5.615	0
N–MoS_2–NH_3–A_1	−0.05	2.823	1.670	2.417	2.403	Metal	5.642	0
N–O–MoS_2	X	X	1.605	2.449	2.393	Metal	6.640	0
N–O–MoS_2–CO–D_1	−0.02	2.725	1.629	2.446	2.389	Metal	5.570	0
N–O–MoS_2–CO_2–D_1	−0.02	2.955	1.619	2.446	2.392	Metal	5.650	0
N–O–MoS_2–NH_3–D_1	−0.09	1.856	1.608	2.449	2.390	Metal	6.104	0

unstable. The adsorption energy E_{ads} is calculated according to eqn (1):

$$E_{ads} = E_{total} - E_{gas} - E_{sub} \quad (1)$$

where E_{ads} is the adsorption energy of system, E_{total} is the energy of the gas-covered MoS_2 surface, E_{gas} is the energy of the isolated gas molecule, E_{sub} is the formation energy of the pristine-MoS_2 or isolated N–MoS_2 (N doped MoS_2), N–O–MoS_2 ((N, O) co-doped MoS_2) systems without adsorbed gas.

For the MoS_2–CO system, the most stable adsorption site is at the bridge site (B) with the carbon atom pointing downward toward the substrate and slightly tilted. The adsorption energy is −0.15 eV and the adsorption distance increases to 3.482 Å (about 16.7%), demonstrating that the pristine MoS_2 and CO interact only weakly, causing the CO molecule to be repelled further away. As a result, the surface corrugation (h) and the longest and shortest Mo–S bond lengths remain almost unchanged with a deviation of only about 0.1%. Essentially, Mo has 6 valence e^- with the atomic configuration $[Kr]4d^5 5s^1$, and S also has 6 valence e^- with the atomic configuration $[Ne]3s^2 3p^4$. Therefore, the Mo–S bonds are mainly formed through the hybridization of the 4d orbitals of Mo and the 3p orbitals of S, making MoS_2 intrinsically saturated in terms of bonding and activation capability. On the other hand, CO, with its strong localization at the C atom and two nonbonding e^- concentrated at the C end, is not sufficient to strongly interact with the stable MoS_2 system, which possesses a bandgap of about 1.77 eV. As a result, CO adsorption on MoS_2 only induces minor perturbations, slightly reducing the bandgap from 1.77 eV to 1.69 eV, while the structure of the system shows no significant changes before and after adsorption. In the case of CO_2 adsorption on pristine-MoS_2, the most stable configuration is located at the top site (A), where the CO_2 molecule lies nearly parallel to the MoS_2 surface and the O–C–O bond angle remains almost unchanged, retaining a nearly linear geometry with an angle of approximately 179.5°. The adsorption energy is −0.15 eV, reflecting weak interaction. The adsorption distance is 3.417 Å, indicating that CO_2 does not form a strong covalent bond with the surface. The surface corrugation (h) is 1.566 Å, almost identical to that of pristine-MoS_2. The Mo–S bond lengths (2.415 and 2.412 Å) differ by less than 0.1%. Similar to the case of CO adsorption, CO_2 is inherently a linear, nonpolar molecule with stable sp and sp^2 hybridizations, in which two strong σ bonds are formed at both ends of the C–O bonds. This structure makes CO_2 highly stable and resistant to rehybridization or the formation of new bonds with the substrate. Combined with the saturated bonding nature of MoS_2, the CO_2 molecule can hardly interact strongly with MoS_2. Therefore, the adsorption process is dominated by weak physical interactions, characterized by small adsorption energy, large adsorption distance, and only minor adjustments in the electronic band structure of the system, as reflected by the negligible reduction of the MoS_2 bandgap. In the case of NH_3 adsorption on pristine-MoS_2, the most stable configuration is obtained at the top (A) site, with one hydrogen atom oriented toward the surface. The molecular dipole aligns so that the N lone pair interacts with the surface molybdenum d orbitals. The calculated adsorption energy is −0.18 eV, which is larger in magnitude than those of CO and CO_2, suggesting a stronger yet still physisorptive interaction. The adsorption distance shortens notably to 2.931 Å, indicating charge donation from NH_3 to the MoS_2 substrate. The H–N–H bond angle remains nearly unchanged at approximately 107°, confirming that the trigonal-pyramidal geometry of NH_3 is largely preserved. The surface corrugation (1.566 Å) and Mo–S bond lengths (2.413/2.412 Å) also remain nearly constant, revealing negligible lattice distortion. This behavior originates from the intrinsic electronic structure of NH_3, where three N–H bonds are formed through sp^3 hybridization, and the N atom retains a nonbonding electron pair with relatively high electronegativity. Such a lone pair readily interacts with the d states of Mo atoms, thereby enhancing the adsorption strength compared with other gas molecules such as CO and CO_2.

Overall, pristine MoS_2 does not interact strongly with CO and CO_2, while it exhibits better interaction with NH_3. Therefore, we introduce N atoms (electron configuration: $1s^2\ 2s^2\ 2p^3$, with 5 valence e^-) into S sites (electron configuration: $[Ne]\ 3s^2\ 3p^4$, with 6 valence e^-), with the aim of breaking the inherent saturation of the triple bond in CO, the double bond in CO_2, and further enhancing the adsorption capability for NH_3. The stable N–MoS_2 structure is shown in Fig. 1(e), with a surface corrugation of 1.595 Å, the longest Mo–S bond elongated to 2.418 Å and the shortest reduced to 2.405 Å. This pronounced change arises from the activation role of the N atom, which creates localized electronic states around the Fermi energy/level (E_f). Specifically, when N substitutes for S in the MoS_2 lattice, the hybridization between the 2p orbitals of N (with high electronegativity and 5 valence e^-, including one lone pair) and the 4d orbitals of Mo together with the remaining 3p orbitals of neighboring S atoms breaks the inherent bonding saturation of pristine-MoS_2. Moreover, the substitution of N, which has 5 valence e^-, in place of S, which has 6 valence e^-, introduces a charge imbalance and disrupts the saturation state compared with pristine-MoS_2. As a consequence, new electronic states emerge near the E_f, leading to the narrowing or even complete disappearance of the bandgap, thereby driving the system from a semiconductor to a metallic state with a direct contribution from the doped N atom. This also suggests that heteroatom doping with higher electron density and greater electronegativity can enhance the activation capability of the system. Furthermore, these localized states act as intermediaries, improving charge donation and acceptance between gas molecules and the MoS_2 substrate, thus enhancing adsorption efficiency, particularly for e^--rich molecules such as NH_3.

Overall, pristine MoS_2 interacts only weakly with CO and CO_2, whereas NH_3 already exhibits a somewhat stronger, albeit still physisorptive, adsorption. To enhance the surface reactivity, one S atom is substituted with N in N–MoS_2 to perturb the saturated Mo–S bonding network and introduce additional active sites. The optimized N–MoS_2 (Fig. 1(e)) displays a slightly larger surface corrugation (h = 1.595 Å) and asymmetric Mo–S bond lengths of 2.418 and 2.405 Å. These structural distortions originate from the hybridization between N-2p, Mo-4d, and neighboring S-3p orbitals, which generates localized electronic

states around the E_f and drives a semiconductor-to-metal transition. The N-induced states thus act as potential active centers that can mediate charge donation and back-donation between gas molecules and the substrate, particularly for electron-rich species such as NH_3

After N doping, the adsorption characteristics of the pristine-MoS_2 system change significantly. For CO, the most stable adsorption occurs at the valley site with the O atom oriented toward the surface, where the adsorption energy decreases to −0.02 eV compared to −0.15 eV in the pristine-MoS_2, while the adsorption distance remains large at 3.609 Å, indicating weak physisorption. The surface corrugation slightly decreases to 1.558 Å, and the Mo–S bonds remain nearly symmetric at 2.416 Å, confirming that the lattice is scarcely affected. After N doping, the adsorption characteristics of MoS_2 change significantly. The most stable adsorption occurs at the valley site with the O atom oriented toward the surface, where the adsorption energy decreases to −0.02 eV compared to −0.15 eV in pristine-MoS_2, while the adsorption distance remains large at 3.609 Å, indicating a weak physisorption mechanism. The surface corrugation slightly decreases to 1.558 Å, and the Mo–S bonds remain nearly symmetric at 2.416 Å, confirming that the lattice is scarcely affected. This can be explained by the fact that the N doping concentration is still relatively low (1/12), such that the activation role of N is insufficient to break the strong hybridized bonds within CO. On the other hand, although N has relatively high electronegativity with the potential to enhance the activation capability of MoS_2, its electron count is not large enough ($Z = 7$) to readily exchange charge and thereby disrupt the strong bonds of CO.

For CO adsorption on N–MoS_2, however, the interaction remains intrinsically weak. The most stable configuration is located at the valley site, with the O atom oriented toward the surface. The adsorption energy decreases in magnitude from −0.15 eV on pristine-MoS_2 to only −0.02 eV, while the equilibrium adsorption distance remains relatively large at 3.609 Å. In parallel, the surface corrugation is slightly reduced to 1.558 Å and the Mo–S bonds remain nearly symmetric at 2.416 Å, indicating that the host lattice experiences only negligible structural perturbation. This subdued response can be ascribed to the relatively low N-doping concentration (1/12 of the S sites) together with the robustness of the internal C–O bond: although N substitution introduces localized states near the E_f, their density and spatial extent are insufficient to strongly couple with the highly localized σ and π orbitals of CO. As a result, CO adsorption on N–MoS_2 still resides in a physisorption regime with minimal electronic and structural rearrangement.

For CO_2, the most stable adsorption site remains at the top, with the molecule lying nearly parallel to the surface and retaining its linear geometry with an O–C–O angle of approximately 179°, the adsorption energy reaches only −0.02 eV, and the distance increases to 3.643 Å compared to 3.417 Å in the pristine case. The surface corrugation changes minimally to 1.559 Å, while the Mo–S bonds vary slightly between 2.416 and 2.414 Å, confirming weak physisorption. Similar to CO, CO_2 is even more difficult to activate because of its linear, nonpolar nature, high chemical inertness, and the strong thermodynamic stability of its C–O bonds. This stability originates from the sp and sp^2 hybridizations of the carbon atom in CO_2, which form very strong σ and π bonds that are hardly broken under the influence of the MoS_2 surface already saturated in bonding. Therefore, even with N doping to generate localized electronic states and enhance activation capability, the interaction of CO_2 with the MoS_2 substrate remains highly limited, and the adsorption process is restricted to weak physisorption with small adsorption energy and nearly unchanged band structure.

In the case of NH_3, the most stable configuration is also at the top site with one H atom pointing downward, where the adsorption energy decreases to −0.05 eV instead of −0.18 eV in the pristine system, but the adsorption distance shortens to 2.823 Å compared to 2.931 Å. The H–N–H bond angle remains close to 107°, preserving the trigonal pyramidal geometry, while the surface corrugation increases significantly to 1.670 Å and the Mo–S bonds become asymmetric with values of 2.417 and 2.403 Å, reflecting local lattice distortion around the N dopant site. Thus, although the adsorption energies of CO, CO_2, and NH_3 on N–MoS_2 remain very small, indicating that the mechanism is still dominated by physisorption, compared with the pristine system, the presence of N introduces pronounced structural and charge redistribution effects, particularly in the case of NH_3. This can be explained by the intrinsic nature of the NH_3 molecule, which adopts a trigonal pyramidal geometry with three N–H bonds formed through sp^3 hybridization between the 2s orbital and the three 2p orbitals of the N atom. In addition, N retains a lone pair of e^- localized on the remaining sp^3 orbital that does not participate in bonding. The combination of the N's relatively high electronegativity and this lone pair enable NH_3 to readily donate or accept charge with the d states of Mo atoms on the surface. On the other hand, N doping significantly disrupts the inherent saturation of the system, thereby enhancing its interaction with the NH_3 molecule, which already showed potential adsorption on pristine-MoS_2. With the additional activation role introduced by the doped N, the interaction becomes even stronger and more favorable. This confirms the important role of N doping in fine-tuning the adsorption properties of MoS_2 and provides the basis for co-doping strategies aimed at further enhancing gas sensing performance.

However, the adsorption strength of the N-doped NH_3 system remains limited, as the calculated adsorption energies for CO, CO_2, and NH_3 are all relatively small. To address this limitation, the strategy of N and O co-doping was further investigated to enhance the adsorption and sensing performance. The N with 5 valence e^- (e^- configuration: $1s^2\ 2s^2\ 2p^3$) and O with 6 valence e^- (electron configuration: $1s^2\ 2s^2\ 2p^4$) were simultaneously substituted at S sites, which also possess 6 valence e^- (e^--configuration: [Ne] $3s^2\ 3p^4$). This combination is expected to create a synergistic effect in which N atoms provide new active sites and enhance charge transfer, while O atoms with high electronegativity induce local lattice distortion and strengthen the bonding capability with gas molecules. The stable N–O–MoS_2 structure is illustrated in Fig. 1(i), showing a surface corrugation of 1.608 Å, higher than 1.564 Å in pristine-

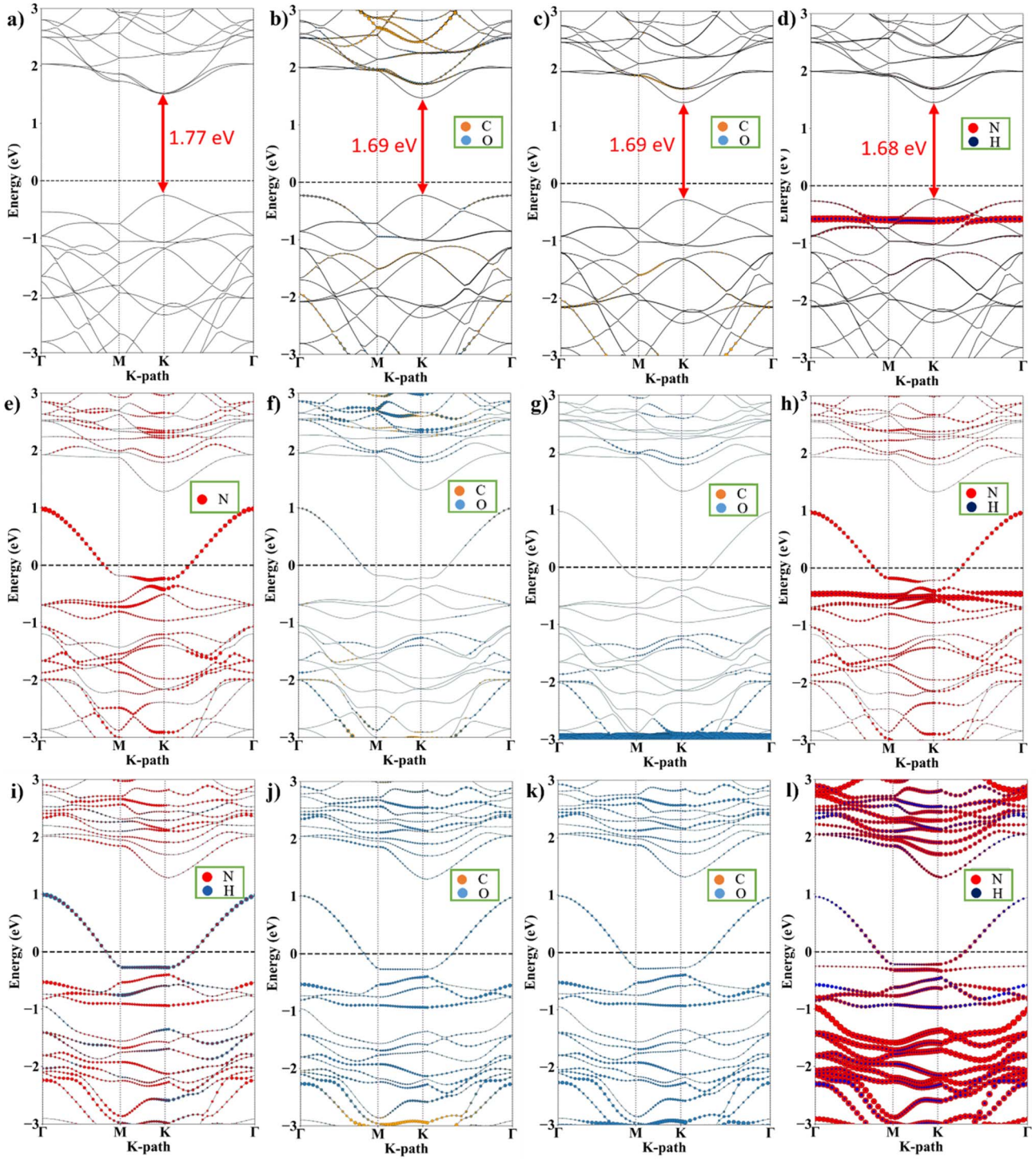

Fig. 2 The non-magnetic atom-projected band structures of (a) pristine-MoS_2, (b) MoS_2–CO–B_1, (c) MoS_2–CO_2–A_1, (d) MoS_2–NH_3–A_1, (e) N–MoS_2, (f) N–MoS_2–CO–D_1, (g) N–MoS_2–CO_2–A_1, (h) N–MoS_2–NH_3–A_1, (i) N–O–MoS_2, (j) N–O–MoS_2–CO–D_1, (k) N–O–MoS_2–CO_2–D_1, (l) N–O–MoS_2–NH_3–D_1. Orange, sky blue, red, and navy circles represent the contributions from C, O, N, and H atoms, respectively.

MoS_2 but lower than 1.670 Å in N–MoS_2. The longest Mo–S bond is elongated to 2.449 Å, while the shortest contracts to 2.390 Å, a larger distortion compared with both pristine (2.413/2.412 Å) and N–MoS_2 (2.418/2.405 Å). Notably, the bandgap completely disappears, and the system remains metallic, as in the case of N doping, indicating that N and O co-doping induces even stronger modifications in the electronic properties of the material compared with both pristine and N doped systems. After co-doping, the adsorption characteristics of MoS_2 undergo significant changes. For CO, the most stable configuration occurs when the molecule tilts slightly toward the surface with the carbon atom pointing downward. The adsorption energy is

−0.02 eV, smaller than that of pristine-MoS_2 (−0.15 eV) and equivalent to that of N–MoS_2 (−0.02 eV), but the adsorption distance shortens considerably to 2.725 Å compared with 3.482 Å in pristine and 3.609 Å in N–MoS_2. This indicates that CO still binds weakly but approaches closer to the surface due to the co-doping effect. The surface corrugation reaches 1.629 Å, higher than both pristine and N–MoS_2, while the Mo–S bonds distort significantly with values of 2.446 and 2.389 Å. For CO_2, the most stable adsorption site is located at the valley position, where the molecule retains a nearly linear O–C–O bond angle of 179.6°. The adsorption energy is calculated to be −0.02 eV, while the adsorption distance shortens to 2.955 Å compared with 3.417 Å on pristine-MoS_2 and 3.643 Å on N–MoS_2. The surface corrugation is 1.619 Å, and the Mo–S bonds exhibit asymmetric distortion (2.446/2.392 Å), indicating stronger local lattice deformation. In the case of NH_3, the most stable configuration occurs at the top site with one H atom oriented toward the surface. The adsorption energy increases noticeably to −0.09 eV, compared with −0.18 eV for pristine MoS_2 and −0.02 eV for N–MoS_2, demonstrating a significant enhancement in binding strength upon N–O co-doping. The adsorption distance decreases markedly to 1.856 Å, much shorter than 2.931 Å in pristine-MoS_2 and 2.823 Å in N–MoS_2, reflecting a significantly stronger molecule–surface interaction. The H–N–H bond angle remains nearly constant at ∼107°, confirming that the trigonal-pyramidal geometry of NH_3 is preserved. The surface corrugation is 1.608 Å, lower than that of N–MoS_2 but higher than the pristine surface, while the Mo–S bonds exhibit pronounced distortion (2.449/2.390 Å). These structural variations arise from the synergistic effect of N and O atoms, which induce substantial charge redistribution when simultaneously substituting two S atoms in the lattice. Such a cooperative electronic perturbation enhances charge transfer between the adsorbate and substrate, sufficient to weaken the stability of CO and CO_2 through orbital hybridization among Mo-4d, N-2p, and O-2p states. As a result, the adsorption distance of CO and CO_2 reduces from ∼3 Å to 2.725 Å. However, the corresponding adsorption energy remains low (−0.02 eV), indicating that the interaction is primarily driven by charge transfer and can be characterized as weak chemisorption. Overall, compared with pristine and singly doped systems, (N, O) co-doping markedly shortens the adsorption distance of CO, CO_2, and NH_3, strengthens the binding of NH_3, and induces stronger lattice deformation, demonstrating the crucial role of (N, O) co-doping synergy in tuning adsorption behavior and enhancing the gas-sensing potential of MoS_2. Besides, it is worthy to note that the calculated magnetic moment of the all studied configurations are equal zero (Table 1), evidencing the non-magnetic feature of these systems. The determined non-magnetic feature results in the non-splitting of spin-up and spin-down components in their band structures and density of states (DOSs) as well as other quantities in later discussion.

3.2. Electronic band structure

To further analyze the electronic properties of MoS_2, we investigated the electronic band structure of this material. The results are shown in Fig. 2, with the vertical axis representing electronic energy (eV) and the horizontal axis representing the k-path in reciprocal space along the high-symmetry points *Γ*–*M*–*K*–*Γ*. The curves in the diagram represent the allowed electronic states, while the red dashed line at 0 eV marks the E_f. As shown in Fig. 2(a), the pristine-MoS_2 is a direct bandgap semiconductor, with the valence band maximum (VBM) and conduction band minimum both located at the *K* point, giving a bandgap of about 1.67 eV. The bands are clearly distributed, with no defective states appearing within the gap, reflecting the ideal semiconducting nature of the system. To evaluate the gas adsorption ability of MoS_2 for potential applications in toxic gas sensors, we further examined the changes in the band structure upon adsorption of CO, CO_2, and NH_3, as shown in Fig. 2(b–d). For the MoS_2–CO system (Fig. 2(b)), the direct bandgap at the *K* point is preserved but decreases to 1.69 eV as the conduction band dispersions are pulled closer to the E_f. Contributions from C and O mainly appear deep below −2 eV or higher above +2 eV, with very weak intensity, reflecting weak interaction. Nonetheless, a faint new dispersion branch emerges very close to the E_f, indicating a slight degree of local orbital hybridization between CO and the MoS_2 states, even though the overall interaction remains weak. Similarly, for the MoS_2–CO_2 system (Fig. 2(c)), the direct bandgap at the *K* point is maintained with a slightly reduced value of 1.69 eV compared with pristine-MoS_2 (1.77 eV). The dispersions near the E_f remain nearly unchanged, while the contributions from C and O are mainly distributed in deeper energy regions below −2 eV or above +2 eV. CO_2 adsorption induces a thin and weak new dispersion branch close to the E_f, but its intensity is too low to affect the electronic nature of the system. This is consistent with the fact that CO_2 is a nearly nonpolar and chemically inert molecule, which interacts only weakly with the already inert MoS_2 surface, leading to physisorption-dominated behavior. The reason is that the hybridization between S-3p_z orbitals and Mo-4d_z orbitals is concentrated at the conduction band minimum, while the overlap of S-3p_{xy} orbitals with Mo-4d_{xy} orbitals dominates the valence band maximum, the effective orbital overlap with the C-2p and O-2p states of CO and CO_2 is nearly negligible. This intrinsic orbital overlap becomes challenging because pristine MoS_2 is a semiconductor with a relatively large bandgap and the E_f lying deep within the gap. As a result, the contribution of C and O to the electronic band structure of MoS_2 is very limited and mainly confined to deep states far from the E_f. Therefore, the role of CO and CO_2 is only weakly manifested by the appearance of a faint dispersion branch at around −0.2 eV, with very modest orbital contributions. Overall, the MoS_2–CO and MoS_2–CO_2 systems remain semiconducting with a direct bandgap of 1.69 eV at the *K* point. Overall, the contributions from C and O lie predominantly deep in the conduction band, with only very limited weight near the E_f. The out-of-plane p_z-orbital hybridization is clearly observed at the *K* point. Meanwhile, the bands below the E_f are distinctly separated and show little mixing; the band edges shift only marginally. These features indicate that CO scarcely alters the electronic nature of MoS_2, and the hybridization remains at the level of weak interaction. In the case of the MoS_2–NH_3 system (Fig. 2(d)), the

direct bandgap at the *K* point narrows to about 1.70 eV, and new dispersions originating from N and H clearly appear in the range from −1 eV to 0 eV. Notably, a new dispersion branch emerges more prominently near the E_f compared with the CO and CO_2 cases, indicating significantly stronger orbital hybridization. This arises from the lone electron pair on the N atom of NH_3, which can overlap with Mo–S electronic states near the E_f. Although the interaction is still physisorption in nature, the higher electronegativity of N enhances the coupling, consistent with the reduced adsorption distance of NH_3 and the presence of N-derived states close to the E_f.

From these results, it is evident that pristine MoS_2 interacts only weakly with CO, CO_2, and NH_3 molecules. While CO and CO_2 adsorption induce only minimal changes and faint dispersion branches near the E_f, NH_3 exhibits stronger orbital hybridization and local modifications of the band structure. This demonstrates that pristine-MoS_2, in its ideal semiconducting form, is not sufficient for direct toxic gas sensing, thereby motivating doping strategies to improve its adsorption and electronic response. In addition, in the N–MoS_2 system (Fig. 2(e)), the substitution of a S atom by a N atom introduces significant changes in the band structure. Unlike the pristine MoS_2, where the direct bandgap at the *K* point is 1.77 eV, the bandgap completely collapses in the presence of N, transforming the material from a semiconductor into a metallic state. The dispersion curves clearly show that the bands cross the E_f, eliminating the gap and forming a 2D electron gas-like system. This metallization originates from the fact that N has only five valence e^- compared to 6 for S, thereby generating e^--deficient sites. The N-2p states strongly hybridize with Mo-4d orbitals and are pinned near the E_f, producing new dispersion branches that cut directly through the E_f energy. As a result, the density of states at the E_f increases substantially, providing abundant active sites for gas adsorption. Accordingly, N induces strongly hybridized N-2p states with Mo-4d, producing dispersion branches that cross the E_f in a two-dimensional e^- gas-like pattern. This hybridization converts MoS_2 from a typical semiconductor into a metal, demonstrating enhanced activation capability and an increased number of mobile e^- within the system. When CO adsorbs on the N–MoS_2 system (Fig. 2(f)), the system retains its metallic character, with the band structure showing electronic bands that continue to cross the E_f without reopening a bandgap.

The contributions from C and O remain very weak, appearing mainly in the valence band between −2 and −1 eV and in the conduction band around +2 eV, far from the E_f. A faint dispersion branch associated with CO appears near Fermi energy, but its intensity is too small to produce significant hybridization. Therefore, although N doping introduces e^--deficient active sites, at a concentration of 1/12 this effect is not strong enough to govern the interaction with CO. As a result, the band structure changes only minimally compared with the N–MoS_2 without gas adsorption. The key reason is that the interaction of the out of plane p_z orbitals only touches the band manifold very shallowly, yielding negligible spectral weight. Moreover, the faint CO induced branches contribute either too deep in the conduction or valence regions, or only minimally near the E_f, so the overall hybridization remains weak. Consequently, the adsorption efficiency is insignificant, even though the charge transfer is somewhat larger than in the case of CO on the pristine substrate. Similarly, CO_2 adsorption on N–MoS_2 (Fig. 2(g)) maintains the metallic nature of the system. The dispersion curves continue to cross the E_f almost unchanged from the bare N-doped case, with C and O contributions remaining weak and far from the Fermi energy, mainly below −2 eV and above +2 eV. A very faint dispersion branch appears near the E_f, reflecting limited orbital overlap. This behavior arises from the nearly nonpolar nature of CO_2, whose linear geometry cancels the dipole moment and makes the molecule chemically inert. Although N doping generates e^--deficient sites and provides active centers, at the low concentration of 1/12 the number of such sites is not sufficient to induce strong hybridization with the stable linear structure of CO_2. Therefore, the adsorption mechanism remains dominated by weak charge transfer and physisorption. In contrast, NH_3 adsorption on N–MoS_2 (Fig. 2(h)) produces a marked difference. The system preserves its metallic character, but additional prominent dispersion branches originating from the N and H atoms of NH_3 appear very close to the E_f (from −1 eV to 0 eV). These branches are much stronger than those in the CO and CO_2 cases, confirming significant orbital hybridization. This arises from the molecular structure of NH_3, which contains three N–H bonds and a lone electron pair on the N atom. The lone pair overlaps effectively with the e^--deficient Mo–N active sites generated by doping, thereby forming stable hybridized states close to the E_f. Even at the relatively low doping concentration of 1/12, the number of active sites is sufficient to create substantial orbital overlaps, enhancing the electronic response of the system. Overall, while CO and CO_2 adsorption on N–MoS_2 remains weak and does not significantly alter the metallic band structure, NH_3 adsorption generates strong dispersion branches near the E_f, indicating a much higher degree of hybridization. This result highlights the role of N doping in breaking the saturated Mo–S bonding network, inducing metallization, and providing active sites that selectively strengthen interaction with NH_3. Thus, N–MoS_2 exhibits superior sensitivity and selectivity toward NH_3 compared with CO and CO_2, confirming its potential as a toxic gas sensor.

On the other hand, (N, O) co-doping enhances the interaction between the substrate and the gas. As observed in Fig. 2(i), the band structure shows little difference from the N doped case. This indicates that (N, O) co-doping does not significantly disrupt the intrinsic structural characteristics of the system, thus preserving the overall band dispersion. However, co-doping introduces new active centers that facilitate interaction and charge transfer, while O contributes to the redistribution of electronic states within the band structure. As a result, the interaction between the substrate and the gas molecules changes noticeably, with CO, CO_2, and NH_3 exhibiting discernible contributions to the band structure across a wide energy range. Although these contributions are not large, they suggest potential activation of additional features and improvements in key gas sensor metrics such as sensitivity, electronic sensitivity, and selectivity. The high electronegativity of O draws gas molecules closer, especially CO and NH_3,

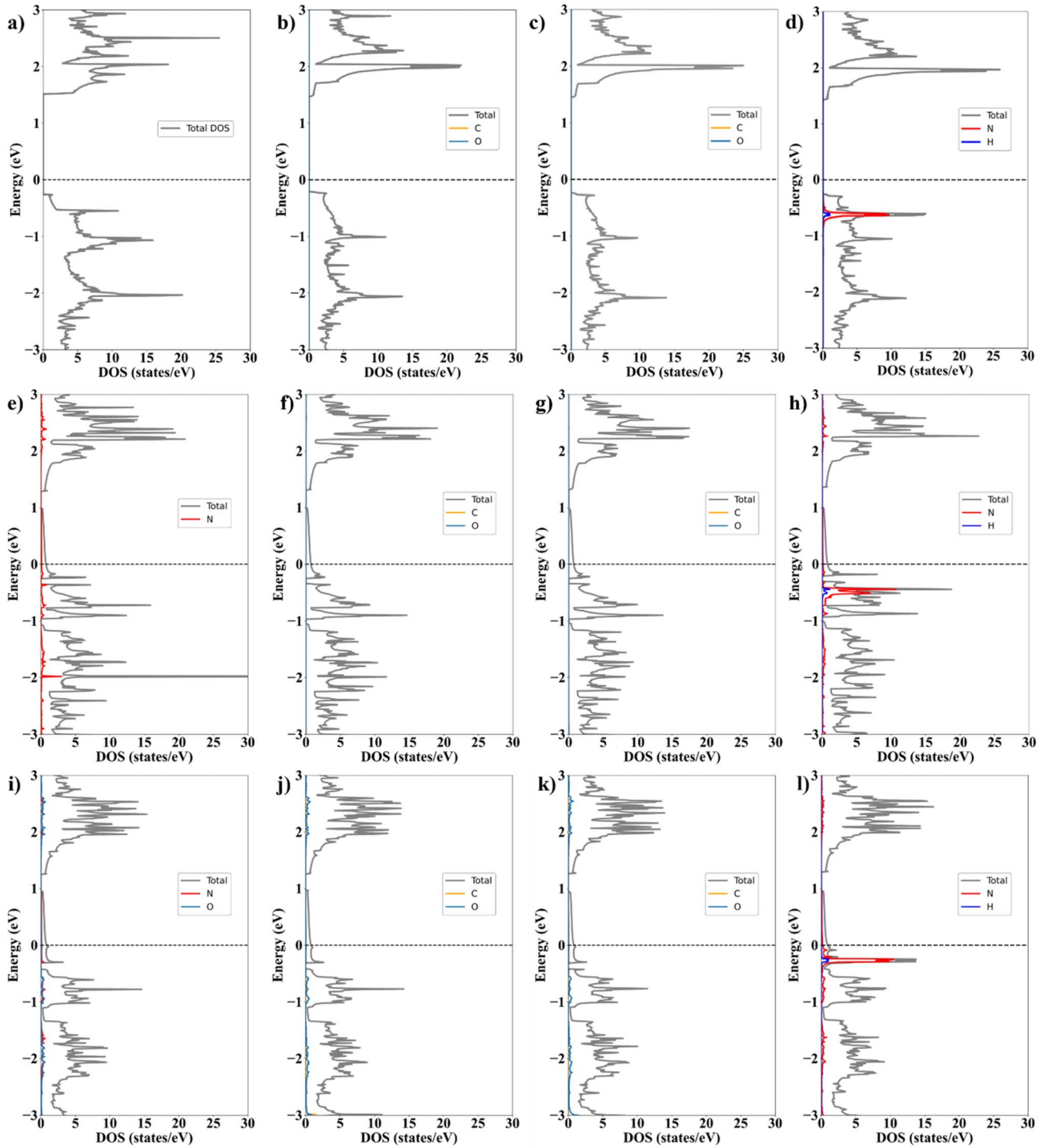

Fig. 3 The non-magnetic atom-projected DOSs of (a) pristine-MoS_2, (b) MoS_2–CO–B_1, (c) MoS_2–CO_2–A_1, (d) MoS_2–NH_3–A_1, (e) N–MoS_2, (f) N–MoS_2–CO–D_1, (g) N–MoS_2–CO_2–A_1, (h) N–MoS_2–NH_3–A_1, (i) N–O–MoS_2, (j) N–O–MoS_2–CO–D_1, (k) N–O–MoS_2–CO_2–D_1, (l) N–O–MoS_2–NH_3–D_1. Gray, orange, sky blue, red, and navy circles represent the contributions from total, C, O, N, and H atoms, respectively.

through strong polarization. Even the nonpolar CO_2 is partially affected, moving closer and participating in charge transfer and hybridization. The direct contributions of CO, CO_2, and NH_3 to the band structure reveal a clear enhancement in orbital hybridization, with Mo-4d orbitals interacting strongly with N-2p and O-2p states. Overall, while CO and CO_2 adsorption on N–O–MoS_2 still exhibit weak interactions with only faint dispersion branches near the E_f, NH_3 adsorption induces pronounced new electronic states directly at the Fermi energy. These findings demonstrate that N and O co-doping not only strengthens the metallic character of MoS_2 but also produces a synergistic effect that substantially enhances its adsorption

capability and electronic response toward NH_3. Therefore, N–O–MoS_2 exhibits superior sensitivity and selectivity toward NH_3 compared with both pristine and N doped systems, highlighting its strong potential as a potential material for toxic gas sensing applications.

3.3. Density of states

To validate the band structure results, we further analyzed the atom–projected density of states (DOS) of the pristine-MoS_2, N–MoS_2, and N–O–MoS_2 systems together with their adsorption systems for CO, CO_2, and NH_3, as illustrated in Fig. 3. For the N–MoS_2 system (Fig. 3(e)), the bandgap collapses completely, transforming the material from a semiconductor into a metallic state. The DOS display a finite density of states at the E_f, with a very intense peak of about 50–55 states per eV located around −2 eV. This feature originates from strong hybridization between N-2p and Mo-4d orbitals, indicating that N substitution introduces e^--deficient sites and significantly increases the density of available active states. Upon CO adsorption (Fig. 3(f)), the system maintains its metallic nature, with only very weak contributions from C and O atoms, appearing far from the E_f at deep valence (below −2 eV) and high conduction states (above +2 eV). A faint branch is observed near the E_f, but its intensity is too small to induce strong orbital overlap, confirming that the interaction remains weak. Similarly, CO_2 adsorption (Fig. 3(g)) leaves the metallic character essentially unchanged, with negligible contributions from C and O close to the E_f. In contrast, NH_3 adsorption (Fig. 3(h)) produces pronounced new states between −1 and 0 eV, directly adjacent to the E_f. These states arise from the lone pair e^- on the N atom in NH_3, which effectively hybridize with the e^--deficient Mo–N active sites. As a result, the DOS near the E_f increases substantially, reflecting stronger orbital hybridization compared with CO and CO_2. In the case of N–O–MoS_2 (Fig. 3(i)), the metallic nature is further enhanced, with a denser DOS distribution around the E_f compared to the N–MoS_2. This behavior results from the synergistic effect of N and O, where N generates e^--deficient sites and O, with its higher electronegativity, induces local lattice distortions and withdraws charge density, thereby generating additional electronic states pinned near the E_f. When CO is adsorbed (Fig. 3(j)), the system remains metallic, but a new branch from C and O atoms appears closer to the E_f compared with the N–O–MoS_2, indicating slightly stronger orbital interaction. For CO_2 adsorption (Fig. 3(k)), a faint but clearer contribution from C and O emerges near the E_f, suggesting that enhanced surface polarization due to O incorporation improves orbital overlap, although the overall interaction remains weak. In sharp contrast, NH_3 adsorption on the N–O–MoS_2 (Fig. 3(l)) produces very strong new states exactly at the E_f, much more pronounced than in both pristine and N–MoS_2. These peaks originate from N and H orbitals in NH_3 strongly hybridizing with Mo–N–O active centers, which explains the much shorter adsorption distance and stronger binding energy observed in this system. Overall, DOS analysis reveals that CO and CO_2 interact only weakly across all three systems, though their contributions become slightly more evident in the N–O–MoS_2. By contrast, NH_3 consistently induces new states close to the E_f, with the most significant enhancement observed in the N–O–MoS_2. This finding highlights the critical role of co-doping in amplifying the metallic character of MoS_2 and creating a synergistic effect that significantly improves sensitivity and selectivity toward NH_3, positioning N–O–MoS_2 as a highly promising candidate for high-performance toxic gas sensors. In the N–MoS_2 (Fig. 3(e)), the bandgap collapses completely, transforming the material from a semiconductor into a metallic state. The DOS shows a finite value at E_f, with a strong peak (∼50–55 states per eV) located around −2 eV, originating from strong hybridization between N-2p and Mo-4d orbitals. This clearly demonstrates that N substitution introduces e^--deficient sites and significantly enhances the density of available active states. Upon CO adsorption (Fig. 3(f)), the DOS maintains its metallic character, with contributions from C and O remaining extremely weak and located far from the E_f (below −2 eV and above +2 eV). Only a faint additional branch appears near the E_f, indicating limited orbital overlap and confirming that CO still interacts very weakly. A similar situation is observed for CO_2 adsorption (Fig. 3(g)), where the DOS retains the metallic nature of the N–MoS_2 and the C/O contributions remain negligible near the E_f. In contrast, NH_3 adsorption (Fig. 3(h)) produces pronounced new states from −1 to 0 eV, directly adjacent to the E_f. These features arise from the lone-pair e^- of N in NH_3 overlapping effectively with the e^--deficient Mo–N sites, leading to stronger orbital hybridization. This enhanced response indicates that N–MoS_2 interacts more selectively and strongly with NH_3 than with CO or NH_3. As for the N–O–MoS_2 (Fig. 3(i)), the metallic character is further enhanced, exhibiting a denser and broader DOS distribution across the E_f compared with the N doped counterpart. The pronounced states near E_f originate from the synergistic effect of N and O, where N introduces e^--deficient sites while O, owing to its higher electronegativity, induces local lattice distortions and withdraws charge density, thereby generating additional states pinned close to the E_f. Upon CO adsorption (Fig. 3(j)), the system retains its metallic nature, but weak new features arising from C and O atoms appear closer to E_f than in the N doped case, suggesting slightly stronger orbital interaction. Moreover, for the case of N–O–MoS_2–CO_2 (Fig. 3(k)), a small but clearer contribution from C and O emerges near the E_f, reflecting enhanced polarization induced by O incorporation; nevertheless, the overall interaction remains weak. In sharp contrast, N–O–MoS_2–NH_3 (Fig. 3(l)) produces strong new states exactly at the E_f, much more intense than those observed in both pristine-MoS_2 and N–MoS_2. These peaks arise as the N and H orbitals of NH_3 strongly hybridize with Mo–N–O active centers, which accounts for the shorter adsorption distance and higher adsorption energy.

In addition, the contribution of N is markedly enhanced compared with pristine MoS_2 and the N-doped system, and the density of states immediately near the E_f increases to nearly 13 states per eV, highlighting the role of O *via* its higher electronegativity in improving adsorption capability by strengthening surface polarization and orbital overlap. Taken together, the DOS results demonstrate that while CO and CO_2 contribute only weakly across all systems, their interaction improves slightly in

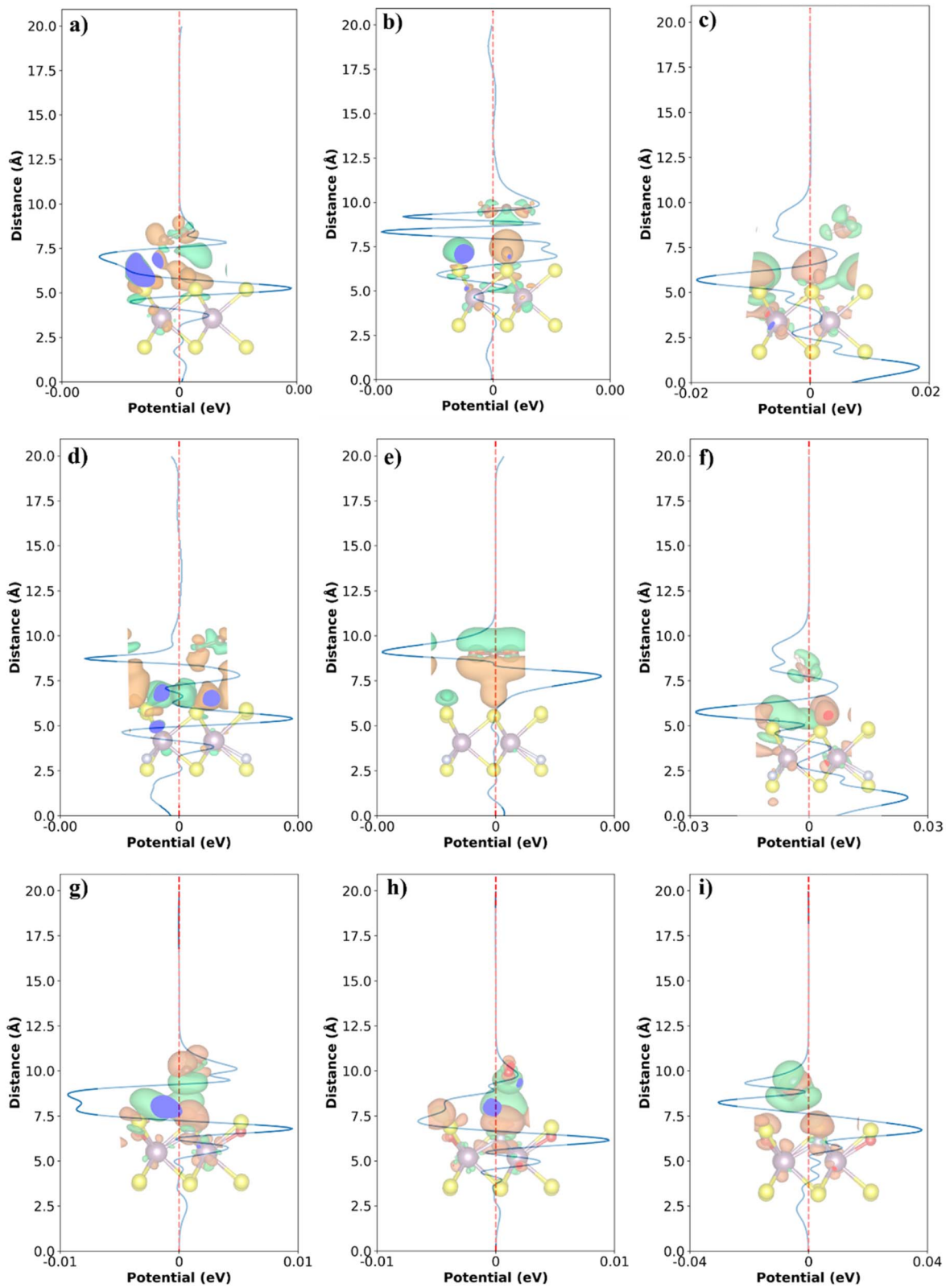

Fig. 4 Spatial charge density difference and planar-averaged electrostatic potential along the *z*-direction of (a) MoS_2–CO–B_1, (b) MoS_2–CO_2–A_1, (c) MoS_2–NH_3–A_1, (d) N–MoS_2–CO–D_1, (e) N–MoS_2–CO_2–A_1, (f) N–MoS_2–NH_3–A_1, (g) N– O–MoS_2–CO–D_1, (h) N– O–MoS_2–CO_2–D_1, (i) N–O–MoS_2–NH_3–D_1. The green regions represent charge depletion, while the orange regions indicate charge accumulation. The flat potential profile is responsible for the vacuum space.

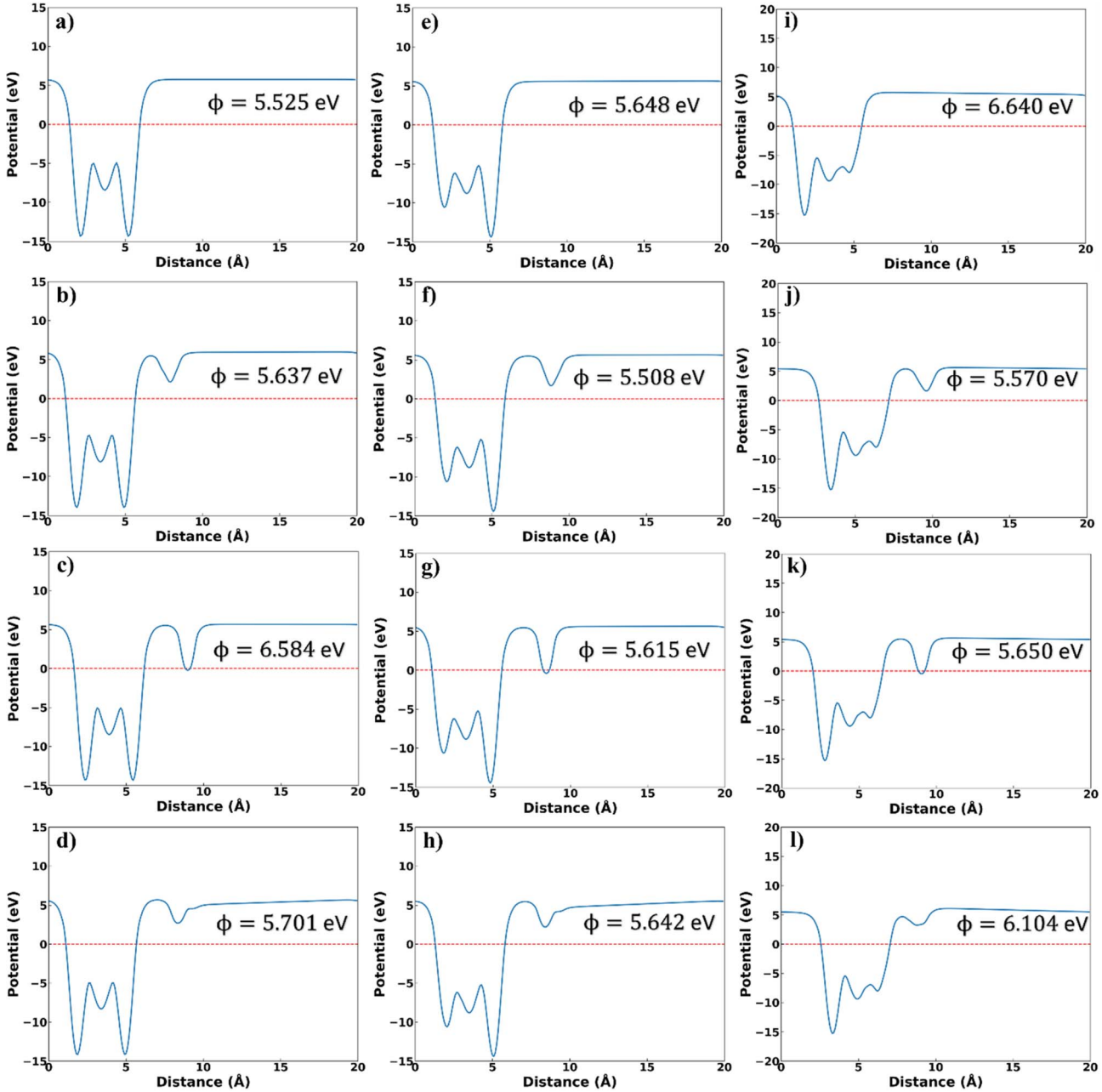

Fig. 5 The work function (ϕ) along the z-direction of (a) pristine-MoS_2, (b) MoS_2–CO–B_1, (c) MoS_2–CO_2–A_1, (d) MoS_2–NH_3–A_1, (e) N–MoS_2, (f) N–MoS_2–CO–D_1, (g) N–MoS_2–CO_2–A_1, (h) N–MoS_2–NH_3–A_1, (i) N–O–MoS_2, (j) N– O–MoS_2–CO–D_1, (k) N– O–MoS_2–CO_2–D_1, (l) N– O–MoS_2–NH_3–D_1.

the N–O–MoS_2. On the other hand, consistently induces new states near the E_f for NH_3 case, with the strongest response observed for the N–O–MoS_2. This confirms that N–O–MoS_2 creates a synergistic effect that not only enhances the metallic nature of MoS_2 but also amplifies its sensitivity and selectivity toward NH_3, making N–O–MoS_2 a highly promising candidate for advanced gas sensing applications.

3.4. Charge density difference

To determine the nature of the adsorption process, the charge difference profile along the z-axis was analyzed, as illustrated in Fig. 4. The charge density difference (CDD) reveals charge transfer between atoms and is crucial for elucidating interatomic interactions at the atomic scale, particularly in doped or adsorbed systems. Regions of charge accumulation appear as orange areas surrounding the atoms, while green areas indicate charge depletion; accompanying this is the plot of the planar averaged electrostatic potential along the z axis. As shown in Fig. 4(a) and (b) for MoS_2–CO and MoS_2–CO_2, the variation in electrostatic potential difference remains nearly constant along the z-axis, clearly confirming that CO and CO_2 do not interact with pristine-MoS_2 that the adsorption mechanism is purely

physisorption. This clearly indicates that the interaction mechanism of the MoS_2–CO and MoS_2–CO_2 are governed mainly by Mo-4d and S-3p hybridization and very weak physisorption, and that the contribution to the electronic properties is dominated by charge exchange weakly.

In contrast, for MoS_2–NH_3 (Fig. 4(c)), the electrostatic potential difference fluctuates slightly, by about 0.02 eV, near the interface between the MoS_2 surface and the NH_3 molecule. This indicates a weak interaction between NH_3 and MoS_2. Nevertheless, NH_3 still contributes noticeably to the band structure and the density of states, mainly through the N atom. This can be rationalized by the lone pair on N and hybridization, which together enhance the electronic impact of NH_3. Furthermore, N doping, which is expected to modulate charge exchange within the MoS_2 substrate, does not significantly enhance the adsorption capability, as the electrostatic potential differences for N–MoS_2–CO and N–MoS_2–CO_2 remain nearly zero. However, N doping slightly improves the adsorption of NH_3, as indicated by an increase in the potential difference from $\pm$0.02 to $\pm$0.03 eV for N–MoS_2–NH_3. The donor and acceptor regions are distributed rather uniformly but exhibit a small potential amplitude, indicating that the role of N in generating e^--deficient centers is valid; nevertheless, activation through the charge exchange pathway remains limited, as reflected by the increased adsorption distance and the minimal contribution of gas molecules to the band structure and density of states. This result is consistent with the intrinsic characteristics of N as a dopant, which possesses a limited electron population in the relevant subshells and a moderately high, though not extreme, electronegativity. As a result, at a doping concentration of 1/12, N induces charge exchange, but only weakly.

More importantly, (N, O) co-doping plays a crucial role in substantially enhancing both adsorption strength and charge exchange behavior. Specifically, N–O–MoS_2–CO (Fig. 4(g)) exhibits a pronounced electrostatic potential variation of approximately $\pm$0.01 eV localized around S, N, and O dopant atoms, indicating a strong e^--accepting tendency and suggesting that N–O–MoS_2 is highly sensitive to CO molecules. In the case of CO_2 (Fig. 2(h)), (N, O) co-doping significantly improves adsorption compared with pristine-MoS_2 or N–MoS_2, increasing the potential variation from nearly 0 to $\pm$0.01 eV. Similarly, for NH_3 (Fig. 4(i)), (N, O) co-doping raises the average electrostatic potential difference to about $\pm$0.04 eV, exceeding that of pristine and N–MoS_2. Overall, (N, O) co-doping enhances CO adsorption, improves CO_2 adsorption. Although NH_3 adsorption on N–O–MoS_2 is stronger than on pristine and N–MoS_2, the adsorption energies and bond distances still place the interaction in a strengthened physisorption regime with enhanced charge transfer rather than true chemisorption.

3.5. Selectivity analysis

On the other hand, the variation in work function (ϕ) between the gas-adsorbed surface and the pristine surface serves as a key indicator for evaluating gas-sensor sensitivity (Table 1). Specifically, the ϕ represents the minimum energy required to release an electron from the material surface into vacuum and is expressed as[58] eqn (2):

$$\phi = E_{vac} - E_f \quad (2)$$

where E_{vac} is the vacuum level (the electrostatic potential value in the far-vacuum region above the surface, where the potential becomes flat), and E_f stands for the Fermi level. Conversely, if the ϕ of the system after gas adsorption is larger than that of the pristine system, the potential barrier is increased and gas adsorption is less favorable. Therefore, a surface with strong gas-adsorption capability typically shows a negative change in ϕ ($\Delta\phi$) and the more negative $\Delta\phi$ is, the higher the sensitivity to the target gas. The change in work function is calculated by eqn (3):

$$\Delta\phi = \phi_{ads} - \phi_{sub} \quad (3)$$

where ϕ_{ads} denotes the ϕ of the adsorbate-covered system (after gas adsorption), and ϕ_{sub} denotes the ϕ of the pristine substrate (clean surface).

Fig. 5 presents the variation of the electrostatic potential and corresponding ϕ along the z-direction for all pristine, N–MoS_2 and N–O–MoS_2, in which more detailed illustration of the vacuum level (E_{vac}) and Fermi level (E_f) in the ϕ plot is provide in Fig. S4 in the SI. The non-monotonic, drop-then-rise features of the planar-averaged electrostatic potential near the surface arise from the gas-induced interface dipole and disappear in the far-vacuum region, where the potential becomes flat and the vacuum level E_{vac} is defined. For pristine-MoS_2 (Fig. 5(a)), the potential difference between the vacuum level and E_f yields a ϕ of 5.525 eV, which increases upon adsorption to 5.637 eV for CO (Fig. 5(b)), 6.584 eV for CO_2 (Fig. 5(c)), and 5.701 eV for NH_3 (Fig. 5(d)) consistent with the minimal hybridization observed in the band-structure and DOS analyses.

The increased ϕ values upon the CO, CO_2, and NH_3 adsorption imply the limited sensing potential of the pristine-MoS_2. For N–MoS_2 (Fig. 5(e)), its ϕ values at 5.648 eV that slightly decreases upon CO, CO_2, and NH_3 adsorption: *e.g.*, 5.508 eV for CO (Fig. 5(f)), 5.615 eV for CO_2 (Fig. 5(g)) and 5.642 eV for NH_3 (Fig. 5(h)). The minor shifts confirm that N doping enhances surface activity and facilitates localized charge redistribution but remains insufficient to produce strong chemisorptive behavior. In sharp contrast, the N–O–MoS_2 (Fig. 5(i)) exhibits a much higher intrinsic ϕ of 6.640 eV, reflecting the strong electronegativity of O atoms and increased e^--withdrawing ability. Upon the target gases adsorption, the ϕ decreases significantly to 5.570 eV for CO (Fig. 5(j)), 5.650 eV for CO_2 (Fig. 5(k)), and 6.104 eV for NH_3 (Fig. 5(l)), revealing pronounced charge transfer from the adsorbed molecules to the substrate.

The negative $\Delta\phi$ shift highlights the synergistic contribution of N and O co-doping, where N donates electrons to form active sites and O enhances interfacial polarization through electron withdrawal. The combined effect substantially strengthens the adsorption-induced potential modulation and improves sensitivity toward all three gases, particularly CO and CO_2. These trends are consistent with the quantitative data summarized in

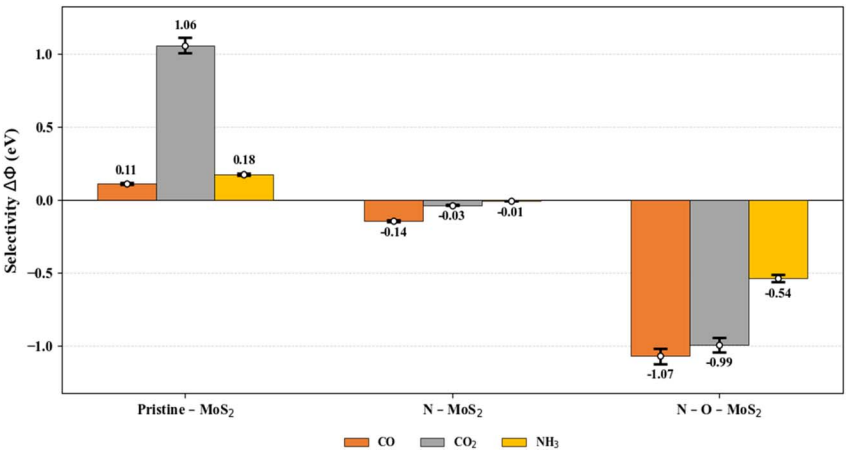

Fig. 6 Comparison of selectivity based on $\Delta\phi$ of the gas-adsorbing substrate and the non-adsorbing substrate.

Table 1, reinforcing that (N, O) co-doping effectively optimizes charge exchange and electronic response for enhanced gas-sensing performance.

Particularly, the sensitivity to the target gases based on the calculated $\Delta\phi$ values (Table 1) is illustrated in Fig. 6, in which the more negative $\Delta\phi$ values indicate the higher sensitivity. It should be mentioned that the positive $\Delta\phi$ values mean poor sensitivity. As a result, the pristine MoS_2 system shows the positive $\Delta\phi$ values with all target gases that indicate its poor sensitivity, limiting its sensing potential. Upon N–MoS_2 and N–O–MoS_2 exhibit the negative $\Delta\phi$ values for all gases, whereas the latter possesses more significant negative $\Delta\phi$ values than that of the former. This evidences the N–O–MoS_2 is identified as the most effective platform to detect the target gases among the other ones, especially for CO and CO_2 with the more significant negative $\Delta\phi$ values at -1.07 eV and -0.99 eV compared with -0.54 eV of NH_3, respectively.

3.6. Electrical sensitivity

To further and more objectively assess the sensitivity of the doped systems upon gas adsorption, we examined the energy-dependent difference in electronic conductivity based on the

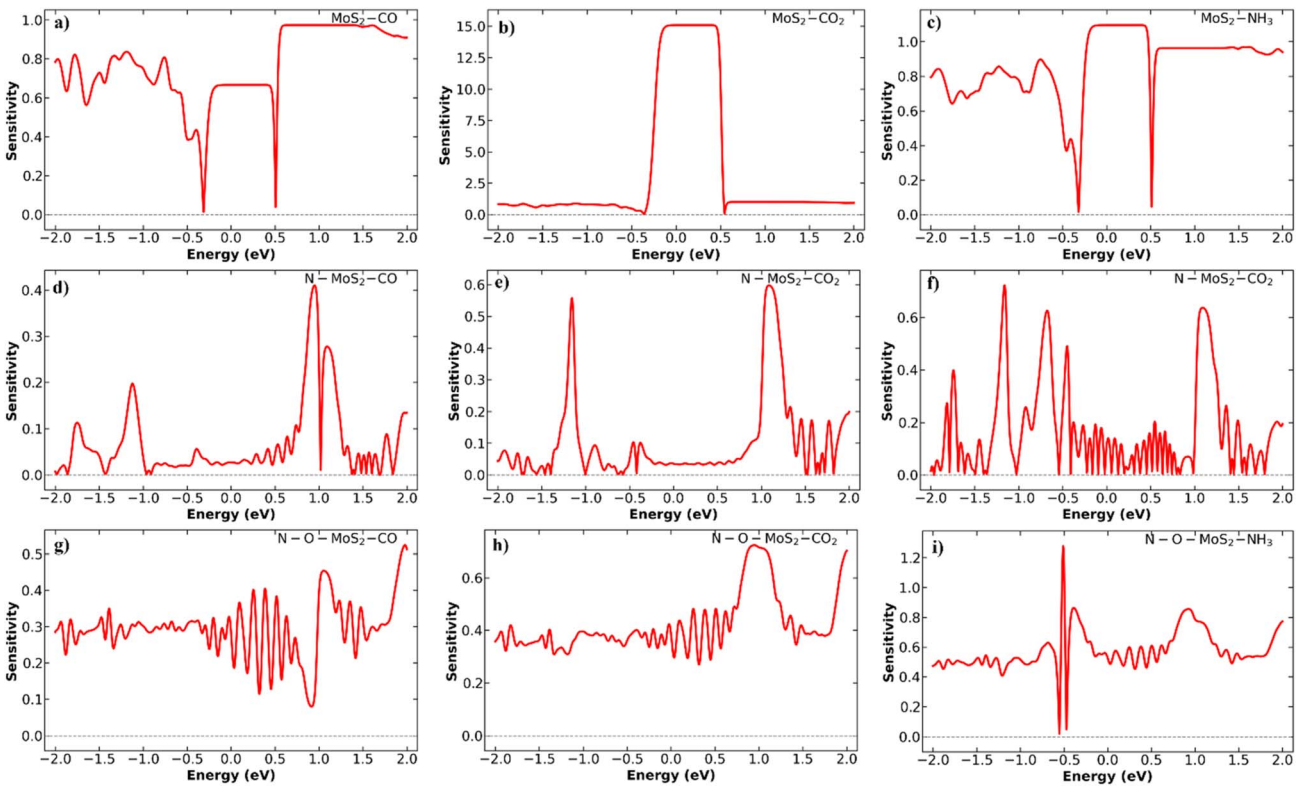

Fig. 7 The electronic conductivity changes for pristine-MoS_2, N–MoS_2 and N–O–MoS_2 absorbed CO (a, d and g), CO_2 (b, e and h) and NH_3 (c, f and i), respectively.

Boltzmann formalism (Fig. 7). Specifically, the electronic conductivity change is defined as the difference in conductivity between the adsorbed system and the non-adsorbed system, according to the following expression (eqn (4)):[59]

$$|\Delta\sigma| = \left|\frac{\sigma_{ads} - \sigma_{sub}}{\sigma_{sub}}\right| \quad (4)$$

Here, σ_{ads} denotes the electrical conductivity of the gas-adsorbed system, and σ_{sub} denotes the conductivity of the pristine substrate.

For the pristine-MoS_2 in Fig. 7(a), the difference in electronic conductivity is very clear and is almost independent of the energy level near the E_f within the range −0.23 to 2 eV, as the curve of the difference is nearly flat. This means that the change in conductivity of the gas-adsorbed system relative to pristine-MoS_2 is essentially constant in that region. In addition, the peaks are irregularly scattered in the band-energy range from −2 to −0.23 eV. This indicates that CO adsorption suppresses internal charge-transfer processes in the system, leading to poor electrical sensitivity, with a difference of about 60–100% across the band structure. By contrast, the inertness of CO_2 toward the MoS_2 substrate is even more evident in Fig. 7(b): the conductivity difference reaches up to 1500% relative to pristine-MoS_2, and the lack of variation in the difference throughout the surveyed band-energy range shows that CO_2 scarcely interacts with MoS_2. This is consistent with the structural, electronic, and selectivity analyses in Fig. 6, where the change in ϕ for CO_2 is the largest. Similarly, NH_3 exhibits weak sensitivity on MoS_2, much like CO, as the electronic conduction change is nearly constant.

On the other hand, the role of N is pronounced, N doping redistributes the conductivity over the entire band-energy range. However, the peaks of the electronic conductivity change remain rather sparse; the highest peaks are mainly located at relatively deep energies around −1.2 eV and 1.0 eV, with maxima of about 40%. In addition, the remaining peaks cluster around the E_f with modest differences (<6%). This shows that CO becomes more sensitive on the N–MoS_2 substrate, but not dramatically so consistent with the previous conclusions. In a similar vein, N doping partially mitigates the inertness of CO_2 by redistributing the band-energy structure with more peaks scattered throughout. However, as in the CO case, the largest peaks, up to about 60% difference are concentrated around −1.2 eV and 1.1 eV, while the others around the E_f have differences below 10%. This again suggests that destabilizing the CO_2 molecule is difficult; thus, although N improves MoS_2's electrical sensitivity to CO_2 to some extent, the enhancement is still limited. A notable highlight appears for NH_3 adsorption in Fig. 7(f), the difference peaks are distributed very evenly with relatively strong intensities, and the highest differences range from about 40% up to 70%. Moreover, the peaks around the E_f increase markedly compared with the CO and CO_2 cases, reaching ∼20%. This provides a clear and encouraging signal regarding both sensitivity and selectivity for NH_3 on N–MoS_2.

Furthermore, the effect of co-doping with N and O is clearly manifested through the stability of the conductivity difference. As seen in Fig. 7(g), the difference between peaks is evenly and widely distributed across the entire band-energy range from −2 to 2 eV; the largest peaks differ only slightly from the others and are almost uniform, typically ranging from 30% to 40%. This indicates very high electrical sensitivity to CO across most of the band-energy range and at different energies, which fully agrees with the selectivity mapping examined in Fig. 6 for N–O–MoS_2–CO. In addition, CO_2 also shows high electrical sensitivity, with average differences of about 35–50% across most energies in the band structure, and the largest peaks reaching ∼70% around 1 eV. Altogether, N–O–MoS_2 demonstrates high sensitivity to CO_2, again consistent with the selectivity results in Fig. 6. Finally, for NH_3 on the co-doped substrate, the sensitivity is very high compared with the CO and CO_2 cases: the charge-difference values average 45–60% across most energies, including around the E_f, and the highest peaks range from ∼80% to over 120% at energies very close to the E_f (around −0.5 eV). This indicates excellent electrical sensitivity of N–O–MoS_2 toward NH_3.

Overall, these results indicate that the intrinsic MoS_2 lattice exhibits limited charge transfer and weak orbital coupling with adsorbed gas molecules, leading to poor electrical sensitivity. The N doping partially mitigates this limitation by introducing e^--deficient centers that enhance local charge redistribution, thereby improving the electronic response. More importantly, the simultaneous incorporation of N and O further amplifies this effect through synergistic electronic modulation. The coexistence of N and O not only enhances surface polarization and carrier density near the E_f but also facilitates stronger orbital hybridization with the adsorbed species. Consequently, N–O–MoS_2 exhibits substantially improved sensitivity and selectivity, particularly toward NH_3, where the combined effects of charge donation and electron withdrawal are maximized.

4. Conclusion

First-principles DFT calculations were conducted to elucidate how N doping and (N, O) co-doping tune the structural, electronic, and sensing characteristics of MoS_2 toward CO, CO_2, and NH_3 gases. Pristine-MoS_2 exhibits weak physisorption with adsorption distances of about 3.6 Å and negligible charge transfer due to the fully saturated Mo-4d and S-3p orbitals. The N doping introduces e^--deficient sites that slightly enhance charge redistribution and improve adsorption, particularly for NH_3 with an adsorption energy of −0.05 eV. In contrast, (N, O) co-doping induces a strong synergistic effect that fundamentally reconstructs the electronic structure of MoS_2. Dual dopants enhance Mo-4d/N-2p/O-2p orbital hybridization and create donor–acceptor charge bridges, converting semiconducting MoS_2 into a metallic, polarization-active system with superior carrier transport. The adsorption distances decrease notably to 2.73 Å for CO, 2.96 Å for CO_2, and 1.86 Å for NH_3, while the adsorption energy for NH_3 increases to −0.09 eV, indicating a strengthened physisorption regime with enhanced charge transfer. Moreover, (N, O) co-doping leads to a significant reduction in ϕ and a uniform distribution of conductivity-change peaks, exceeding 120% for NH_3 and 70% for CO_2, reflecting enhanced charge-transfer efficiency and excellent

electronic sensitivity. These enhancements stem from the synergistic modulation of surface polarization and orbital hybridization induced by N and O dopants. Overall, dual (N, O) co-doping provides an effective pathway for optimizing the interfacial electronic coupling, sensitivity, and selectivity of MoS_2, establishing a robust theoretical foundation for developing high-performance 2D gas sensors with improved response and long-term operational stability.

Author contributions

Khiet An Vuong: investigation, data curation, visualization, writing – original draft. Nguyen Hai Dang: visualization, writing – reviewing and editing. Le Phuong Truong: formal analysis, writing – reviewing and editing. Minh-Thuan Pham: formal analysis, writing – reviewing and editing. D. M. Hoat: formal analysis, writing – reviewing and editing. Minh-Triet Dang: software, writing – reviewing and editing. Guo-Ping Chang-Chien: writing – reviewing and editing. Duy Khanh Nguyen: Supervision, conceptualization, investigation, methodology, validation, resources, funding acquisition, writing – reviewing and editing.

Conflicts of interest

The authors declare that they have no known competing financial interests or personal relationships that could have appeared to influence the work reported in this paper.

Data availability

The data that supports the findings of this study are available within the article.

Supplementary information (SI) is available. See DOI: https://doi.org/10.1039/d5ra08975a.

Acknowledgements

Duy Khanh Nguyen gratefully acknowledges the support of Van Lang University.

References

1 W. M. Alberts, Indoor Air Pollution: NO, NO_2, CO, and CO_2, *J. Allergy Clin. Immunol.*, 1994, **94**, 289–295, DOI: 10.1053/ai.1994.v94.a56007.

2 S. S. Taha, S. Idoudi, N. Alhamdan, R. H. Ibrahim, R. Surkatti, A. Amhamed and O. F. Alrebei, Comprehensive Review of Health Impacts of the Exposure to Nitrogen Oxides (NO_x), Carbon Dioxide (CO_2), and Particulate Matter (PM), *J. Hazard. Mater. Adv.*, 2025, **19**, 100771, DOI: 10.1016/j.hazadv.2025.100771.

3 S. N. Behera, M. Sharma, V. P. Aneja and R. Balasubramanian, Ammonia in the Atmosphere: A Review on Emission Sources, Atmospheric Chemistry and Deposition on Terrestrial Bodies, *Environ. Sci. Pollut. Res.*, 2013, **20**, 8092–8131, DOI: 10.1007/s11356-013-2051-9.

4 J. B. A. Gomes, J. J. P. C. Rodrigues, R. A. L. Rabêlo, N. Kumar and S. Kozlov, IoT-enabled gas sensors: Technologies, applications, and opportunities, *J. Sens. Actuator Netw.*, 2019, **8**(4), 57, DOI: 10.3390/jsan8040057.

5 D. K. Nguyen, D. Q. Hoang and D. M. Hoat, Exploring a Silicene Monolayer as a Promising Sensor Platform to Detect and Capture NO and CO Gas, *RSC Adv.*, 2022, **12**(16), 9828–9835, DOI: 10.1039/d2ra00442a.

6 D. K. Nguyen, D. M. Hoat, A. Bafekry, V. Van On, J. F. Rivas-Silva, M. Naseri and G. H. Cocoletzi, Theoretical Prediction of the PtOX (X = S and Se) Monolayers as Promising Optoelectronic and Thermoelectric 2D Materials, *Phys. E*, 2021, **131**, 114732, DOI: 10.1016/J.PHYSE.2021.114732.

7 N. T. T. Tran, D. K. Nguyen, S. Y. Lin, G. Gumbs and M. F. Lin, Fundamental Properties of Transition-Metals-Adsorbed Graphene, *ChemPhysChem*, 2019, **20**(19), 2473–2481, DOI: 10.1002/cphc.201900614.

8 A. Chaves, J. G. Azadani, H. Alsalman, D. R. da Costa, R. Frisenda, A. J. Chaves, S. H. Song, Y. D. Kim, D. He, J. Zhou, A. Castellanos-Gomez, F. M. Peeters, Z. Liu, C. L. Hinkle, S. H. Oh, P. D. Ye, S. J. Koester, Y. H. Lee, P. Avouris, X. Wang and T. Low, Bandgap Engineering of Two-Dimensional Semiconductor Materials, *npj 2D Mater. Appl.*, 2020, **4**, 29, DOI: 10.1038/s41699-020-00162-4.

9 V. Van On, D. M. Hoat, D. K. Nguyen, R. Ponce-Pérez, T. V. Vu, J. F. Rivas-Silva and G. H. Cocoletzi, Fluorinating the Graphene-like BeO Monolayer: A Spin-Polarized First Principles Study of the Electronic, Magnetic and Optical Properties, *Phys. Scr.*, 2020, **95**(10), 105806, DOI: 10.1088/1402-4896/abb698.

10 D. K. Nguyen, J. Guerrero-Sanchez, T. V. Vu, R. Ponce-Pérez and D. M. Hoat, Electronic and Magnetic Properties of the WSO Janus Monolayer Engineered by Intrinsic Defects, *Surf. Interfaces*, 2022, **32**, 102114, DOI: 10.1016/J.SURFIN.2022.102114.

11 D. K. Nguyen, C. V. Ha, J. Guerrero-Sanchez and D. M. Hoat, Doping Janus MoSSe Monolayer with Al/Ga and P/As Atoms, and Their Clusters: Effective Methods for the Band Structure and Magnetism Engineering, *RSC Adv.*, 2025, **15**(7), 5096–5104, DOI: 10.1039/d5ra00561b.

12 X. Tian, S. Wang, H. Li, M. Li, T. Chen, X. Xiao and Y. Wang, Recent Advances in MoS_2-Based Nanomaterial Sensors for Room-Temperature Gas Detection: A Review, *Sens. Diagn.*, 2023, **2**(2), 361–381, DOI: 10.1039/d2sd00208f.

13 D. K. Nguyen, D. Q. Hoang and D. M. Hoat, Exploring the Sensing Ability of B– and Si–Doped WS2 Monolayer toward CO and NO Gas, *Int. J. Quantum Chem.*, 2022, **122**(15), e26916, DOI: 10.1002/qua.26916.

14 J. K. Lyu, S. F. Zhang, C. W. Zhang and P. J. Wang, Stanene: A Promising Material for New Electronic and Spintronic Applications, *Ann. Phys.*, 2019, **531**(10), 1–12, DOI: 10.1002/andp.201900017.

15 D. M. Hoat, K. D. Vo, N. T. T. Tran, Q. D. Ho, M. T. Dang, H. A. Huy, D. T. Nhan and D. K. Nguyen, Feature–Rich Fundamental Properties of Hydrogen-Adsorbed Armchair Graphene Nanoribbons: Insights from First–Principles

Calculations, *RSC Adv.*, 2025, **15**(33), 27139–27153, DOI: 10.1039/d5ra04327a.
16 T. N. Tran, *et al.*, Enhanced Sodium-Ion Intercalation and Migration in Boron/Carbon-Doped WS2/Graphene Bilayers: Insights from Electronic Structure Calculations, *RSC Adv.*, 2025, **15**(30), 24575–24587, DOI: 10.1039/d5ra04616e.
17 Z. Ni, Q. Liu, K. Tang, J. Zheng, J. Zhou, R. Qin, Z. Gao, D. Yu and J. Lu, Tunable Bandgap in Silicene and Germanene, *Nano Lett.*, 2012, **12**(1), 113–118, DOI: 10.1021/nl203065e.
18 N. T. T. Tran, G. Gumbs, D. K. Nguyen and M. F. Lin, Fundamental Properties of Metal-Adsorbed Silicene: A DFT Study, *ACS Omega*, 2020, **5**(23), 13760–13769, DOI: 10.1021/acsomega.0c00905.
19 S. Huang, W. Kang and L. Yang, Electronic Structure and Quasiparticle Bandgap of Silicene Structures, *Appl. Phys. Lett.*, 2013, **102**(13), 1–5, DOI: 10.1063/1.4801309.
20 D. K. Nguyen, N. T. T. Tran, Y. H. Chiu and M. F. Lin, Concentration–Diversified Magnetic and Electronic Properties of Halogen-Adsorbed Silicene, *Sci. Rep.*, 2019, **9**(1), 1–15, DOI: 10.1038/s41598-019-50233-w.
21 D. K. Nguyen, R. P.-P. Hoang, J. Guerrero-Sanchez and D. M. Hoat, Surface functionalization of graphene-like boron arsenide monolayer: a first-principles study, *J. Phys.: Condens. Matter*, 2024, **36**, 055001.
22 T. Y. Mi, D. M. Triet and N. T. Tien, Adsorption of Gas Molecules on Penta-Graphene Nanoribbon and Its Implication for Nanoscale Gas Sensor, *Phys. Open*, 2020, **2**, 100014, DOI: 10.1016/j.physo.2020.100014.
23 D. K. Nguyen, N. T. T. Tran, Y. H. Chiu, G. Gumbs and M. F. Lin, Rich Essential Properties of Si–Doped Graphene, *Sci. Rep.*, 2020, **10**(1), 1–16, DOI: 10.1038/s41598-020-68765-x.
24 D. T. Nhan, N. V. A. Duy, N. C. Ben, D. K. Nguyen, Y. A. Zulueta, N. To Van, V. B. T. Phung, N. V. Nghia, M. T. Nguyen and M. T. Dang, Unraveling the Electronic Mechanisms of Transition Metal and Fluorine Co-doping for Enhanced Electrochemical Performance in Sodium Lithium Manganese Oxide Cathodes, *Dalton Trans.*, 2025, **54**, 16704–16717, DOI: 10.1039/d5dt00638d.
25 T. N. Tran, T. A. Nguyen, N. Vo, A. Duy, T. L. Nguyen, V. A. Dinh, P. Schall and M. T. Dang, Adsorption of cadmium selenide clusters: A novel approach to enhance solar energy conversion using armchair graphene nanoribbons, *AIP Adv.*, 2024, **14**, 035020, DOI: 10.1063/5.0187458.
26 T. N. Tran, N. V. A. Duy, N. H. Hieu, T. A. Nguyen, N. T. Van, T. V. B. Phung, Y. A. Zulueta, M. T. Nguyen, P. Schall and M. T. Dang, Electric field enhances the electronic and diffusion properties of penta-graphene nanoribbon anodes in lithium-ion batteries, *RSC Adv.*, 2024, **14**, 33524–33535, DOI: 10.1039/D4RA05464D.
27 J. Y. Damte and H. Ataalite, First-Principles Investigation of Gas Adsorption on Bilayer Transition Metal Dichalcogenides for Sensing Toxic Gases, *Results Phys.*, 2025, **70**, 108183, DOI: 10.1016/j.rinp.2025.108183.
28 C. Patra, V. K. Guna, S. Chakraborty, S. Mondal and Y. Nandakishora, Advances in 2D Transition Metal Dichalcogenide-Based Gas Sensors, *ACS Sens.*, 2025, **10**(9), 6347–6379, DOI: 10.1021/acssensors.5c02126.
29 A. K. Geim and K. S. Novoselov, The Rise of Graphene, *Nat. Mater.*, 2007, **6**(3), 183–191, DOI: 10.1038/nmat1849.
30 A. Dey, Semiconductor Metal Oxide Gas Sensors: A Review, *Mater. Sci. Eng., B*, 2018, **229**, 206–217, DOI: 10.1016/j.mseb.2017.12.036.
31 I. Muhammad, H. Xie, U. Younis, Y. Qie, W. Aftab and Q. Sun, A BN Analog of Two-Dimensional Triphenylene-Graphdiyne: Stability and Properties, *Nanoscale*, 2019, **11**(18), 9000–9007, DOI: 10.1039/C9NR02334H.
32 K. Hussain, U. Younis, I. Muhammad, Y. Qie, Y. Guo, T. Li, H. Xie and Q. Sun, Three-Dimensional Porous Borocarbonitride BC2N with Negative Poisson's Ratio, *J. Mater. Chem. C*, 2020, **8**(44), 15771–15777, DOI: 10.1039/D0TC03832F.
33 U. Younis, F. Qayyum, I. Muhammad, M. Yaseen and Q. Sun, A Stable Three-Dimensional Porous Carbon as a High-Performance Anode Material for Lithium, Sodium, and Potassium Ion Batteries, *Adv. Theory Simul.*, 2022, **5**(9), 2200230, DOI: 10.1002/adts.202200230.
34 U. Younis, I. Muhammad, Y. Kawazoe and Q. Sun, Tuning the Properties of Tetracene-Based Nanoribbons by Fluorination and N-Doping, *ChemPhysChem*, 2019, **20**(21), 2799–2805, DOI: 10.1002/cphc.201900803.
35 U. Younis, I. Muhammad, F. Qayyum, Y. Kawazoe and Q. Sun, A Stable Metallic 3D Porous BPC2 as a Universal Anode Material for Li, Na, and K Ion Batteries with High Performance, *J. Mater. Chem. A*, 2020, **8**(48), 25824–25830, DOI: 10.1039/D0TA10446A.
36 M. J. Szary and P. Radomski, Unveiling the Chemical Underpinnings behind the Enhanced Adsorption Interaction of NO_2 on MoS_2, $MoSe_2$, and $MoTe_2$ Transition Metal Dichalcogenides, *J. Phys. Chem. C*, 2023, **127**(43), 21374–21386, DOI: 10.1021/acs.jpcc.3c05101.
37 X. Li and H. Zhu, Two-Dimensional MoS_2: Properties, Preparation, and Applications, *J. Materiomics.*, 2015, **1**(1), 33–44, DOI: 10.1016/j.jmat.2015.03.003.
38 K. F. Mak, C. Lee, J. Hone, J. Shan and T. F. Heinz, Atomically Thin MoS_2: A New Direct–Gap Semiconductor, *Phys. Rev. Lett.*, 2010, **105**(13), 136805, DOI: 10.1103/PhysRevLett.105.136805.
39 A. Shokri and N. Salami, Gas Sensor Based on MoS_2 Monolayer, *Sens. Actuators, B*, 2016, **236**, 378–385, DOI: 10.1016/j.snb.2016.06.033.
40 S. Zhao, J. Xue and W. Kang, Gas Adsorption on MoS_2 Monolayer from First–Principles Calculations, *Chem. Phys. Lett.*, 2014, **595–596**, 35–42, DOI: 10.1016/j.cplett.2014.01.043.
41 Y. Linghu and C. Wu, Gas Molecules on Defective and Nonmetal–Doped MoS_2 Monolayers, *J. Phys. Chem. C*, 2020, **124**(2), 1511–1522, DOI: 10.1021/acs.jpcc.9b10450.
42 Q. Yue, Z. Shao, S. Chang and J. Li, Adsorption of gas molecules on monolayer MoS_2 and effect of applied electric field, *Nanoscale Res. Lett.*, 2013, **8**, 425, DOI: 10.1186/1556-276X-8-425.

43 T. E. Gber, H. Louis, A. E. Owen, B. E. Etinwa, I. Benjamin, F. C. Asogwa, M. M. Orosun and E. A. Eno, Heteroatoms (Si, B, N, and P) Doped 2D Monolayer MoS_2 for G NH_3 as Detection, *RSC Adv.*, 2022, **12**(40), 25992–26010, DOI: 10.1039/d2ra04028j.

44 F. M. Enujekwu, Y. Zhang, C. I. Ezeh, H. Zhao, M. Xu, E. Besley, M. W. George, N. A. Besley, H. Do and T. Wu, N-Doping Enabled Defect-Engineering of MoS_2 for Enhanced and Selective Adsorption of: CO_2 A DFT Approach, *Appl. Surf. Sci.*, 2021, **542**, 148556, DOI: 10.1016/j.apsusc.2020.148556.

45 Z. Li, D. Zhou and J. Xiangke, Highly Selective Adsorption on Monolayer MoS_2 Doped with Pt, Ag, Au and Pd and Effect of Strain Engineering: A DFT Study, *Sens. Actuators, A*, 2021, **322**, 112637, DOI: 10.1016/j.sna.2021.112637.

46 M. Qu, S. Xu, A. Du, C. Zhao and Q. Sun, Co_2 capture, Separation and Reduction on Boron-Doped, MoS_2 $MoSe_2$ And Heterostructures with Different Doping Densities: A Theoretical Study, *ChemPhysChem*, 2021, **22**(23), 2392–2400, DOI: 10.1002/CPHC.202100377.

47 W. Yin, X. Liu, X. Zhang, X. Gao, V. L. Colvin, Y. Zhang and W. W. Yu, Synthesis of tungsten disulfide and molybdenum disulfide quantum dots and their applications, *Chem. Mater.*, 2020, **32**(11), 4409–4424, DOI: 10.1021/acs.chemmater.0c01441.

48 C. Shen, Y. Q. Chen and W. Zhao, Enhanced VOCs Adsorption on Group VIII Transition Metal–Doped MoS_2: A DFT Study, *Chem. Phys.*, 2025, **589**, 112497, DOI: 10.1016/J.CHEMPHYS.2024.112497.

49 I. J. T. Jensen, A. Ali, P. Zeller, M. Amati, M. Schrade, P. E. Vullum, M. B. Muñiz, P. Bisht, T. Taniguchi, K. Watanabe, B. R. Mehta, L. Gregoratti and B. D. Belle, Direct Observation of Charge Transfer between NO_x and Monolayer b MoS_2 y Operando Scanning Photoelectron Microscopy, *ACS Appl. Nano Mater.*, 2021, **4**, 3319–3324, DOI: 10.1021/acsanm.1c00137.

50 A. Kushwaha, N. R. Bharti, A. Sharma, S. K. Kedia, G. Gupta and N. Goel, Enhanced NO_2 Gas Sensing in Nanocrystalline MoS_2 *via* Swift Heavy Ion Irradiation: An Experimental and DFT Study, *ACS Sens*, 2024, **9**(11), 5966–5975, DOI: 10.1021/acssensors.4c01812.

51 L. J. Kong, G. H. Liu and L. Qiang, Electronic and Optical Properties of O-Doped Monolayer MoS_2, *Comput. Mater. Sci.*, 2016, **111**, 416–423, DOI: 10.1016/j.commatsci.2015.10.001.

52 J. Hafner, Materials simulations using VASP-a quantum perspective to materials science, *Comput. Phys. Commun.*, 2007, **177**, 6–13, DOI: 10.1016/j.cpc.2007.02.045.

53 P. Zhao, H. Wang, Z. Huang, B. Fan, Y. Liu, Z. Yin, Y. Wang, X. Zheng, Y. Deng and X. Fan, High-Throughput Screening of Nitrogen Reduction Reaction on Single Atom@1T′-MoS_2, *Appl. Surf. Sci.*, 2023, **631**, 157480, DOI: 10.1016/j.apsusc.2023.157480.

54 L. O. Wagner, T. E. Baker, E. M. Stoudenmire, K. Burke and S. R. White, Kohn–Sham Calculations with the Exact Functional, *Phys. Rev. B: Condens. Matter Mater. Phys.*, 2014, **90**(4), 045109, DOI: 10.1103/PhysRevB.90.045109.

55 G. Kresse and D. Joubert, From ultrasoft pseudopotentials to the projector augmented-wave method, *Phys. Rev. B: Condens. Matter Mater. Phys.*, 1999, **59**(3), 1758–1775, DOI: 10.1103/PhysRevB.59.1758.

56 K. Wang, K. Ren, Y. Cheng, S. Chen and G. Zhang, The Impacts of Molecular Adsorption on Antiferromagnetic $MnPS_3$ Monolayers: Enhanced Magnetic Anisotropy and Intralayer Dzyaloshinskii–Moriya Interaction, *Mater. Horiz.*, 2022, **9**(9), 2384–2392, DOI: 10.1039/D2MH00462C.

57 S. Ghosh, M. Dey Sarkar, P. Nath and D. Sanyal, An *Ab Initio* Study on the Adsorption of Hydrogen Molecules over Tin Sulfide Monolayer, *Appl. Phys. A*, 2025, **131**(10), 773, DOI: 10.1007/s00339-025-08871-7.

58 A. Kahn, Fermi Level, Work Function and Vacuum Level, *Mater. Horiz.*, 2016, **3**(1), 7–10, DOI: 10.1039/c5mh00160a.

59 J. Prasongkit, V. Shukla, A. Grigoriev, R. Ahuja and V. Amornkitbamrung, Ultrahigh–Sensitive Gas Sensors Based on Doped Phosphorene: A First–Principles Investigation, *Appl. Surf. Sci.*, 2019, **497**, 143660, DOI: 10.1016/j.apsusc.2019.143660.